

RESEARCH ARTICLE | MAY 15 2024

Gravitational modes of convection in water liquid bridges

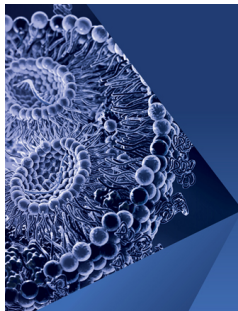
Special Collection: [Overview of Fundamental and Applied Research in Fluid Dynamics in UK](#)

Ahmed Aljanadi (احمد صلاح الدين الجندى) ; Mónica S. N. Oliveira ; Marcello Lappa  



Physics of Fluids 36, 054113 (2024)

<https://doi.org/10.1063/5.0208126>



Physics of Fluids

Special Topic:

Flow and Lipid Nanoparticles

Guest Editors: Richard Braatz and Mona Kanso

[Submit Today!](#)

Gravitational modes of convection in water liquid bridges

Cite as: Phys. Fluids **36**, 054113 (2024); doi: [10.1063/5.0208126](https://doi.org/10.1063/5.0208126)

Submitted: 13 March 2024 · Accepted: 25 April 2024 ·

Published Online: 15 May 2024




View Online



Export Citation



CrossMark

Ahmed Aljanadi (احمد صلاح الدين الجندى), , Mónica S. N. Oliveira, , and Marcello Lappa^{a)} 

AFFILIATIONS

James Weir Fluids Laboratory, Department of Mechanical and Aerospace Engineering, University of Strathclyde, James Weir Building, 75 Montrose Street, Glasgow G11XJ, United Kingdom

Note: This paper is part of the special topic, Overview of Fundamental and Applied Research in Fluid Dynamics in UK.

^{a)} Author to whom correspondence should be addressed: marcello.lappa@strath.ac.uk

ABSTRACT

The modes of pure buoyant (thermogravitational) convection emerging in a liquid bridge of water ($Pr \cong 6.1$), uniformly heated from below and cooled from above are investigated experimentally by means of a microscale facility, a related laser-cut technique (used to illuminate iso-dense tracers dispersed in the liquid) and a particle image velocimetry method. In particular, the following conditions are examined: aspect ratio ($A = \text{length/diameter}$) in the range $0.3 \leq A \leq 0.9$, volume ratio $0.7 \leq S \leq 1.3$, and Rayleigh number spanning the interval from the initial quiescent state up to the development of oscillatory motion. A multitude of patterns is obtained, revealing the coexistence of different branches of steady flows in the space of parameters in the form of multiple solutions. These can evolve into oscillatory states featured by disturbances with the characteristics of standing waves (a kind of rocking motion). The analysis largely relies on a novel approach where the position of the center of the main vortex of buoyant nature established in the liquid bridge is carefully monitored in space. The related trajectory is used to discern the flow spatial degrees of freedom, which are progressively enabled as the temperature difference is increased. It is shown that the effective volume of liquid held by surface tension between the hot and cold walls can have an appreciable impact on the onset of unsteadiness and the related oscillation frequency.

© 2024 Author(s). All article content, except where otherwise noted, is licensed under a Creative Commons Attribution (CC BY) license (<https://creativecommons.org/licenses/by/4.0/>). <https://doi.org/10.1063/5.0208126>

I. INTRODUCTION

For years, the problem of buoyancy convection in cavities and other geometrical configuration having cylindrical symmetry has been of great interest to engineers and scientists due to its ubiquity in technological applications. Experts from diverse fields have considered domains with the cylindrical symmetry for various reasons (which include, but are not limited to, heat exchangers, power and thermal energy storage systems, and materials manufacturing and desalination processes; see, e.g., Muller *et al.*,¹ Crochet *et al.*,² Bennacer *et al.*,³ Arena *et al.*,⁴ Ben Hamid *et al.*,⁵ Azzouz and Hamida⁶).

Leaving aside for a while the related technological implications, the complexity of this specific problem is intriguing to scientists as many factors contribute to shaping it.⁷ These include, among others, the type of fluid considered (Newtonian/non-Newtonian; see, e.g., Borońska and Tuckerman^{8,9} and Lappa and Boaro¹⁰), the thermal behavior of the side boundary (possible paradigms being the cases where it is considered adiabatic or conducting), and the “physical nature” of the lateral boundary itself (be it a “no-slip” wall or a “stress-free” surface).

The case where no solid boundary limits the system from the side may be regarded as a more exotic (or less investigated) variant due to the experimental difficulties, which it typically implies (as we will explain in more detail later). A practically realizable version of a geometry with axial symmetry and stress-free conditions is the so-called “liquid bridge” (LB), namely, a column of liquid suspended by surface tension between two circular concentric disks or rods having the same diameter. This specific configuration has also attracted the attention of academia and industry owing to its relevance to other important technological applications (see, e.g., Kimura and Kitamura,¹¹ Koohpayeh *et al.*,¹² Riemann and Luedge,¹³ Chen and Smith,¹⁴ and Das *et al.*¹⁵).

It was originally introduced in the 1970s as a vehicle for performing experiments dealing with another form of convection, namely, the so-called Marangoni or thermocapillary flow, which is produced when a temperature gradient is applied in a direction parallel to the free liquid–gas interface (the vertical direction in normal gravity^{16,17}). In order to filter out gravitational effects and investigate the undisturbed Marangoni flow, the liquid bridge paradigm has been largely used to conduct

experiments on sounding rockets or other orbiting platforms (where large liquid columns could be obtained; Savino *et al.*¹⁸ and Kang *et al.*¹⁹).

It has also been used to a certain extent in normal gravity conditions (Preisser *et al.*,²⁰ Frank and Schwabe,²¹ Monti *et al.*,²² Ueno *et al.*,²³ Abe *et al.*,²⁴ and Gotoda *et al.*,²⁵ just to cite a few representative examples). Its intrinsic advantages essentially reside in the ability to maximize the ratio between the area of the free surface and that of all the other solid surfaces, thereby providing a good background for the development and observation of surface-tension driven flow (Velten *et al.*²⁶ and Lappa *et al.*²⁷).

Given this premise, pure thermocapillary or mixed Marangoni-buoyant states of convection and related hierarchy of bifurcations are no longer discussed here as they are beyond the scope of this work. Nevertheless, it is worth highlighting that the omnipresent nature of the Marangoni effects in most of existing liquids goes some way to explain the substantial lack of experimental results about the properties of (pure or “dominant”) gravitational convection in liquid columns. While a large amount of literature exists for the cases where a fluid uniformly heated from below and cooled from above is encapsulated in closed cylindrical containers (see, e.g., Touihri *et al.*²⁸), gaps in our understanding start to appear when the alternate LB configuration is considered. No experimental works have been produced to date, given the inherent difficulties related to any attempt made to separate buoyancy convection from the thermocapillary effect when the fluid is heated from below. While large liquid bridges (where buoyancy flow would be dominant) are not possible in normal gravity conditions (owing to gravity, which tends to pull the liquid down), the Marangoni effect typically becomes dominant in micro-scale conditions, thereby preventing researchers from concentrating on, or discerning, the intrinsic features of thermogravitational flow.

As discussed in more detail in Sec. II, we envision something different. In practice, by exploiting a poorly known natural principle (valid for certain fluids only), we filter out the undesired (in this case) presence of Marangoni flow and focus on purely thermal buoyancy effects. While doing so, we also take advantage of some specific features of the liquid bridge configuration, such as the possibility to vary freely its aspect ratio (the ratio of its height and diameter) and the amount of liquid effectively suspended between the supporting disks.

II. GEOMETRICAL CONFIGURATION AND METHODOLOGICAL APPROACH

A. The liquid bridge

As explained in the introduction, as a distinguishing mark with respect to the existing literature on liquid bridges, we concentrate on a situation where the liquid bridge (see Fig. 1) is expected to support buoyancy convection while minimizing fluid motion of a thermocapillary nature. In order to do so, we rely on a peculiar property of water (unknown to the most, but familiar to fluid physicists involved in the experimental investigation of Marangoni flows).

Pure water is known to exhibit a strong Marangoni effect; however, there is evidence that some nano-particles and (especially) *microorganisms* (i.e., bacteria) naturally present in the considered work environment can quickly “contaminate” the free surface (Schwabe, private communication, 2016). Such a localized contamination has essentially no impact on the physical properties of water (density, kinematic viscosity, thermal diffusivity, and even the surface tension itself are not affected); nevertheless, it can dramatically hinder the ability of the fluid to support Marangoni flow, i.e., the ability of the free surface to generate tangential stresses in response to the application of a tangential temperature gradient.

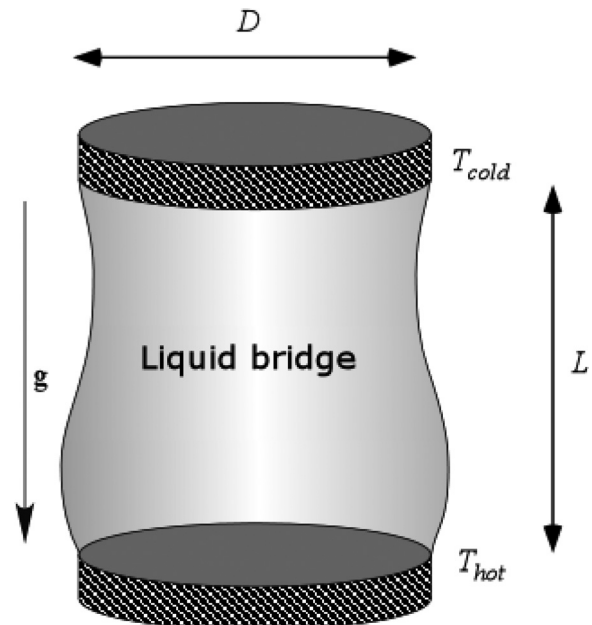


FIG. 1. Sketch of the liquid bridge highlighting relevant variables and related boundary conditions.

Although some investigators are currently trying to unveil the underlying physics in the framework of molecular dynamic (MD) simulations, a precise interpretation for this behavior is still lacking; however, consensus exists that certain immiscible impurities being accumulated along the liquid–air interface somehow interfere with water inter-molecular forces, thereby suppressing the mechanisms by which molecules can freely move in a tangential direction. As a result, surface fluid parcels can be displaced only if the inner layer of liquid in contact with them is moving, and, accordingly, this results in what mathematicians would simply call “stress-free” boundary behavior.

While an experimentalist interested in Marangoni flow would consider this a “drawback,” in the present work, we explicitly take advantage of this property to study the possible modes of purely buoyant flow, i.e., Rayleigh–Bénard (RB) convection emerging in a differentially heated liquid bridge with heating being applied from below.

B. Filtering out thermocapillary effects

Relevant details about the procedure used to verify the effective absence of thermocapillary effects in the considered setup are provided in this section. In this regard, first, we wish to remark that, unlike other studies, where pure water had to be encapsulated in a sterilized and purified gaseous environment in order to allow the Marangoni effect to show up, here no specific countermeasures were taken to prevent the impurities naturally present in the ambient air from contaminating the liquid bridge surface. Second, we also took advantage of another relatively simple concept, that is, the inability of a liquid bridge heated from above to support buoyancy convection.

Put simply, we conducted *experiments* with the liquid bridge *being uniformly heated from above and cooled from below*. In these conditions, the temperature tends to be horizontally stratified along the vertical

direction, therefore leaving room for Marangoni flow. These tests have definitely confirmed the negligible role that surface-tension effects play in the considered dynamics. Indeed, no fluid motion could be observed for a temperature difference as high as 40 K. We wish also to remark that in these tests, the temperature of the supporting disks was set in order to make the mean temperature of the liquid identical to that of the external environment, thereby minimizing the heat exchange between the liquid bridge and the external environment (see Sec. III A for additional details about this simple artifice, which has been instrumental in filtering out buoyant convective modes potentially induced by radial temperature gradients). The outcomes of this *modus operandi* can be seen in Fig. 2, where a snapshot of the liquid bridge with aspect ratio $A = L/D = 0.7$, volume ratio $S \cong 1$, $\Delta T = 40$ K, and disk diameter 5 mm is shown. As the reader will realize by inspecting this figure, the uniform, pattern-less distribution of tracers is indicative of a quiescent state.

It is worth highlighting that all the experiments reported in this study were executed considering liquid bridges held between disks with the same diameter as that shown in Fig. 2, i.e., 5 mm. Although this size is generally considered unsuitable when substances with a relatively small value of the surface tension (σ) are considered (as it results in liquid bridges strongly deformed by gravity for aspect ratios of unit order), it has proven to lead to almost cylindrical liquid bridges in the present case in a relatively extended range of aspect ratios. This has been made possible by another favorable property of water, i.e., the relatively high value of its surface tension with respect to other substances that are liquid and transparent at ambient temperature, i.e., $\sigma \cong 72.8 \times 10^{-3}$ N/m at 20 °C for water, as opposed to, e.g., $\sigma \cong 2.1 \times 10^{-3}$ N/m for silicone oils and $\sigma \cong 2.2 \times 10^{-3}$ N/m for ethanol. For the convenience of the reader, the physical properties of water at ambient temperature are listed in Table I.

C. Characteristic parameters

As usual, the introduction of relevant non-dimensional parameters is beneficial to place the considered problem in a more general context. Such parameters can be synthetically introduced as

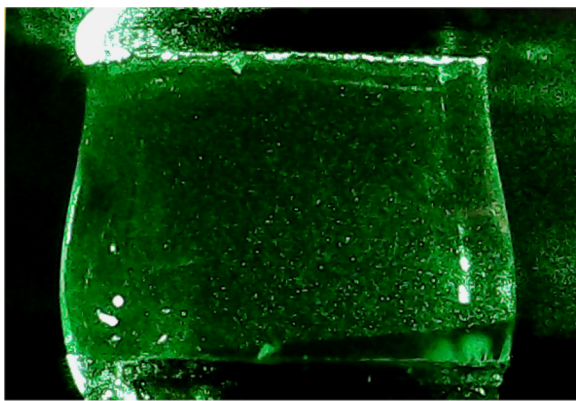


FIG. 2. Snapshot of liquid bridge heated from above and cooled from below ($D = 5$ mm, aspect ratio $A = L/D = 0.7$, volume ratio $S \cong 1$, $\Delta T = 40$ K). No fluid motion (picture taken after 5 min). The volume ratio is defined as the effective volume of the liquid bridge divided by the volume of the cylinder having the same diameter D and height L .

TABLE I. Physical properties of pure water at 20 °C.

Physical property	Dimensional value
Kinematic viscosity (ν)	$10^{-6} \text{ m}^2 \text{ s}^{-1}$
Density (ρ)	10^3 kg m^{-3}
Thermal conductivity (λ)	$0.598 \text{ W m}^{-1} \text{ K}^{-1}$
Specific heat (Cp)	$4.18 \times 10^3 \text{ J kg}^{-1} \text{ K}^{-1}$
Thermal diffusivity (α)	$1.43 \times 10^{-7} \text{ m}^2 \text{ s}^{-1}$
Thermal expansion coefficient (β_T)	$2.07 \times 10^{-4} \text{ K}^{-1}$
Surface tension (σ)	$72.8 \times 10^{-3} \text{ N m}^{-1}$

$$Pr = \frac{\nu}{\alpha}, \quad (1)$$

i.e., the so-called Prandtl number, where ν and α are the liquid kinematic viscosity and thermal diffusivity, respectively. The corresponding Rayleigh number reads

$$Ra = \frac{g\beta_T\Delta TL^3}{\nu\alpha}, \quad (2)$$

where g and β_T are the gravity acceleration and the thermal expansion coefficient, respectively (the reader can refer to Table I for the related values).

The so-called “aspect ratio” of the liquid bridge is non-dimensional (purely geometrical) group, generally defined as²²

$$A = \frac{L}{D}, \quad (3)$$

where L and D are the liquid bridge height and diameter, respectively. Given the absence of solid walls limiting the fluid from the side, an additional relevant degree of freedom is represented by the effective volume of liquid held between the supporting disks (V_{eff}). If the volume of the corresponding cylinder having the same base D and height L is used as a point of reference, another characteristic ratio can be introduced using these two volumes as

$$S = \frac{4V_{eff}}{\pi D^2 L}. \quad (4)$$

As the reader will easily realize, the values of this parameter smaller or larger than one can be readily used to distinguish convex (fat, $S > 1$) from concave (slender, $S < 1$) liquid bridges, respectively.

A complete characterization of the geometrical properties of the liquid bridge, however, also requires consideration of another influential factor that depends on gravity. When the experiments are conducted in normal gravity conditions, the interface of the liquid bridge obviously undergoes some deformation due to the gravitational force, which tends to pull the liquid down. In such circumstances, the final shape of the liquid bridge is representative of the equilibrium conditions, which are finally attained when gravity and the restoring effect of the liquid surface tension (σ) balance each other. These two fundamental forces can be combined into the so-called Bond number:

$$Bo = \frac{\Delta\rho g L^2}{\sigma}, \quad (5)$$

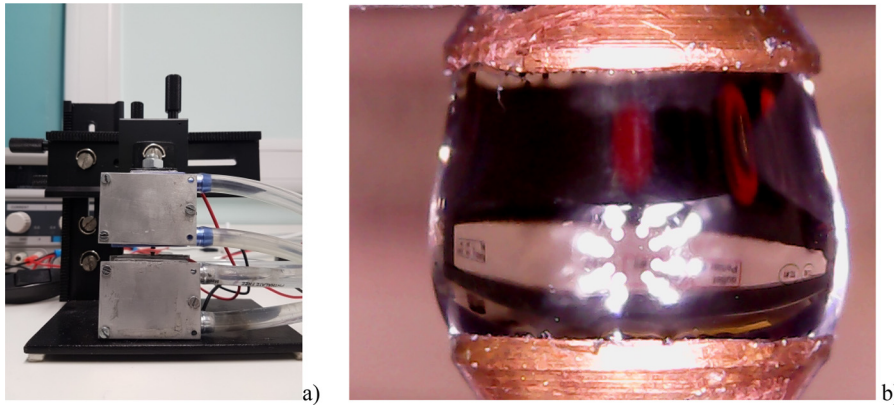


FIG. 3. Microscale facility: (a) front view and (b) enlarged view of the liquid bridge formed between the copper supporting disks.

where $\Delta\rho$ is the density jump between the liquid and the surrounding gas ($\Delta\rho \cong \rho_{\text{liquid}}$). In such a context, the condition $Bo=0$ should be obviously regarded as a limiting condition ideally obtained in the microgravity environment (where given the absence of the gravitational pull, a perfectly cylindrical liquid bridge would be recovered for $S=1$).

D. The microscale facility

The overall experimental setup used for the execution of these experiments can be seen in Figs. 3 and 4.

The liquid bridge is constrained between two opposing copper disks [these being available with a variety of diameters, namely, 2, 3, and 5 mm, see Fig. 3(a)]. These are part of rods, having a total length

(axial extension) of 2.9 cm, which are mounted inside a corresponding hole created in a piece of aluminum (size $4 \times 4 \times 1.1 \text{ cm}^3$), which, in turn, is in contact with a Peltier element having a $4 \times 4 \text{ cm}^2$ size. The Peltier element, in turn, is mounted adjacent to a $4 \times 4 \times 1 \text{ cm}^3$ metal container in which water is recirculated in order to extract heat from the Peltier element itself (Fig. 4). A good thermal contact between all the above-mentioned components is ensured by the application of a special compound (a gel), which prevents a layer of insulating air from being formed between the related surfaces. Water recirculation is forced through the use of external pumps equipped with a relatively small liquid reservoir (MANKd MS-500 Bruhess DC Motor pumps, 12W, 10V, $Q_{\text{max}} 500 \text{ l/h}$, Fig. 5) or using a dedicated thermal bath (Nickel Electro™ Clifton™ Unstirred Digital Water Bath) for the cases where a larger temperature difference is needed.

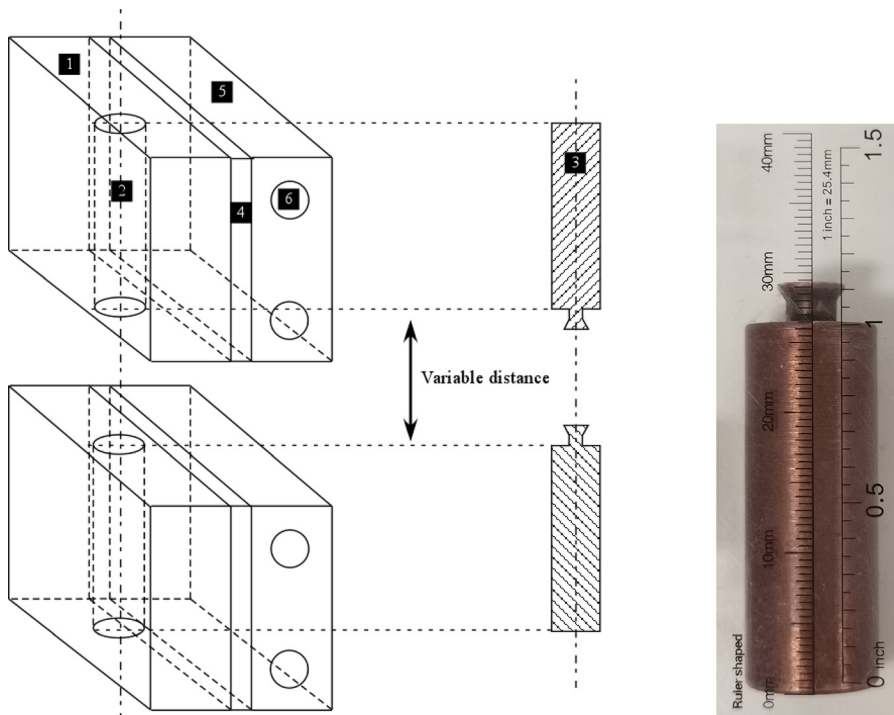


FIG. 4. Sketch of the two sub-assemblies hosting the copper rods with the opposing disks supporting the liquid bridge. (1) Parallelepipedic block of aluminum, (2) hole housing the copper rod, (3) copper rod, (4) Peltier element, (5) reservoir with cooling fluid connected to an external pump, and (6) inlet and outlet sections of the reservoir. The inset is a picture of the copper rod.

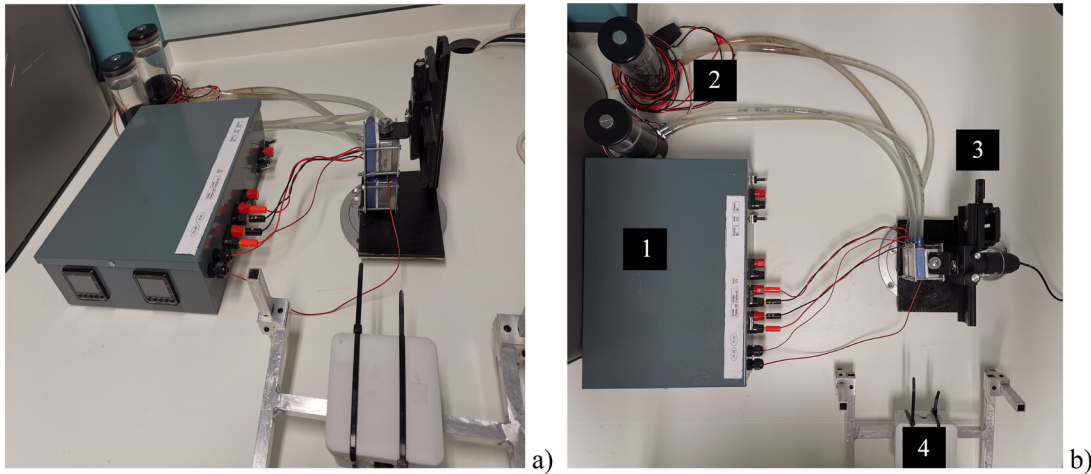


FIG. 5. Overall experimental setup: (a) side view and (b) as seen from above. (1) Thermal control system, (2) pumps, (3) microscale facility, and (4) laser device.

The liquid bridge top disk is surrounded concentrically by a horizontal shield made of plastic material (not shown) used to mitigate the buoyant convection otherwise generated in the air surrounding the liquid bridge and the related radial temperature gradients (following the same approach originally implemented by Velten *et al.*²⁶).

The thermal systems assembly (providing the necessary functionality to induce temperature differences of desired magnitude across the liquid bridge) can be described as follows:

The temperature gradient required to put the fluid in motion is generated by two Peltier modules ($40 \times 40 \times 4 \text{ mm}^3$, 12 V, 6 A). Each of these is connected to a dedicated Omron E5CC temperature controller (accurate to $\pm 0.3^\circ\text{C}$) relying on 1 mm K-type thermocouple. Each of the two thermocouples (providing the temperature controller with the required feedback) is inserted into a small blind hole (1.3 mm diameter) directly created at the basis of the liquid bridge supporting disks (thereby measuring with a very good approximation the temperature effectively established on the disk itself).

Moreover, the temperature controller (Fig. 5) relies on the following principle. The direct current (DC) pulse signals generated by the temperature controller are sent to a solid state relay (SSR)

connected with the Peltier module to form a simple series circuit (Fig. 6). The sinusoidal output of the temperature controller is then transformed into a square wave “on-off” signal used to modulate the voltage supplied to the Peltier devices in order to maintain a desired temperature (the voltage being increased if the temperature is smaller than the desired value and vice versa). More specifically, this is achieved through a proportional-integral-derivative (PID) law.

As outlined before, heat is extracted from each Peltier module using two dedicated pumps. The required voltage (power) for the pumps, the Peltier elements, and the thermal controller itself are provided by a multi-output DC regulated CSI 3005EII power supply, enabling to generate selectively different voltages (in the range between 0 and 30 V) on different independent channels.

Dedicated test activities have led to the conclusion that this system can maintain a constant temperature difference as high as 80°C with the minimum achievable temperature (cold disk) ranging between 0 and 5°C depending on the considered conditions and the maximum being limited by the temperature at which the considered liquid starts to boil (100°C for water).

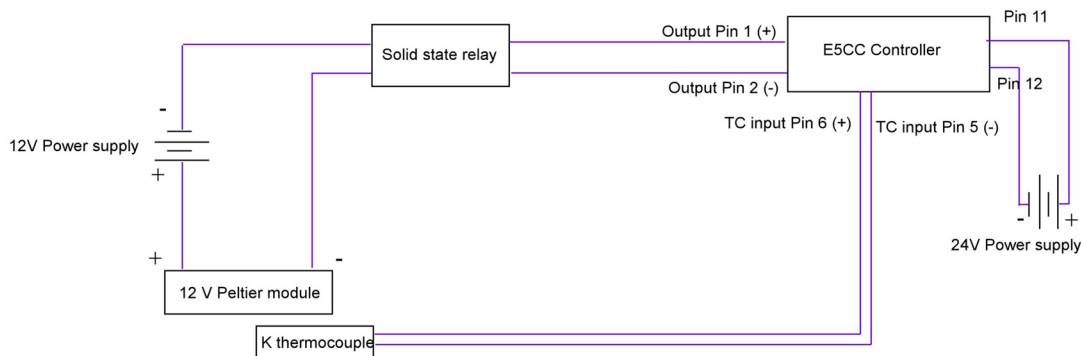


FIG. 6. Circuit diagram of the temperature control circuit of the microscale facility. Overall, there are two such circuits, i.e., one for each Peltier device.

16 May 2024 12:37:44

Technical sheet: Microscale facility

Component	Properties / Performances
Multi/output DC regulated power supply (CSI3005EIII, manufactured by Circuit Specialists Europe)	Output voltage: 0–30 V (adj. continuously) Output current: 0–5 A (adj. continuously) Volt-indication: LED $\pm 1\% \pm 2$ digits Amp-indication: LED $\pm 2\%$
Temperature controller (Omron E5CC)	Accuracy: $\pm 0.3^\circ$
Thermocouple (K type)	Allowed range: -75 to $+250^\circ\text{C}$
Peltier modules	$4 \times 4\text{ cm}^2$, 72 W Temperature range: -10 to 100°C at the outer surface of the piece of metal hosting the copper cylinders with the liquid bridge disks at the end
Cooling system (MANkd MS-500Bruhess DC motor pumps)	12 W, 10 V, Q_{\max} 500 l/h
Laser	Wavelength: $532\text{ nm} \pm 10$ and power max output: $<50\text{ mW}$
Microscope	Resolution: 640×480 pixels, frame rate: 8 frames per s

A digital microscope (Dizzymall 1000 \times Microscope Magnification USB Microscope 8-led Digital Endoscope with Stand) is used to record the motion of tracers dispersed in the considered liquid, which is then stored in the form of high-resolution video files. The tracers are ceramic particles of $50\ \mu\text{m}$ in diameter having a 10^3 kg/m^3 density. A laser with wavelength $532 \pm 10\text{ nm}$ and power max output $<50\text{ mW}$ provides the required illumination, thereby making tracers visible as small green spots against a black background. The positions and relative orientation of both the microscope and light source are set or controlled using fully adjustable support mechanisms. In line with earlier successful attempts for the case of Marangoni flow,^{20,22} the camera is positioned in a direction perpendicular to the “light cut” created using a cylindrical (biconvex) lens to turn the laser beam into a thin light sheet.

The overall microscale facility is mounted on a workbench providing anti-vibration isolation. The horizontal orientation of the experimental setup is verified using a digital inclinometer with an accuracy of 0.01° (Neoteck NTK033-V).

Other relevant aspects of the experimental procedure used to conduct the experiments described in this study are discussed herein.

For all cases of interest, a defined initial amount of liquid has been injected from a dedicated push syringe into the gap between disks to form the liquid bridge with the desired aspect ratio and shape. Before starting each experiment, a snapshot has been taken of the liquid bridge shape (side view) and used as a “reference condition” for the ensuing addition of other liquid to compensate liquid losses due to evaporation

(see, e.g., Gotoda *et al.*,^{25,29} this need being effective for relative large values of the temperature imposed on the hot disk). In addition, the effective amount of liquid held between the supporting disks has been confirmed *a posteriori* through a procedure where the interface shape has been turned into an analytical function (a polynomial expression), which has then been integrated to calculate the volume.

E. The particle image velocimetry technique

An extensive description of the particle image velocimetry (PIVlab) method used to determine the distribution of velocity in the present work can be found in the study by Thielicke and Stamhuis.³⁰ Here, we limit ourselves to recalling the rationale underlying the specific options of this software that we have enabled in order to obtain the results discussed in Sec. III.

Like all the other digital particle image velocimetry (DPIV) methods, PIVlab relies on the differential analysis of particle distribution between a pair of images taken at different (relatively close) instants (the distribution of tracers in the light sheet in the present case). Velocities in the sheet are mathematically derived using the distance that particles cover over the time distance that separates the two considered images. In practice, the algorithm determines the particle displacement for groups of particles through the evaluation of the *cross correlation* of many small sub-images (generally referred to as “interrogation areas”). The process provides the most probable displacement for groups of particles that travel along straight paths. Although this description applies essentially to any DPIV algorithm, there are specific aspects that contribute to make some variants more efficient or reliable than others. In this regard, in addition to the cross correlation process, the so-called image pre-processing and post-processing stages also play a crucial role.

As an example, for the present analysis, before the cross correlation stage, we have used contrast limited adaptive histogram equalization (Pizer *et al.*³¹). In this way, image regions affected by low and/or high exposure have been optimized by spreading out the most frequent intensities of the image histogram to the full range of the data.

In the cross correlation stage, we have used a discrete Fourier transform (DFT), given the related advantages in terms of computational efficiency (Soria³²). The loss of information associated with this approach (typically resulting in an increasing amount of background noise in the correlation matrix, which complicates the detection of the intensity peak and decreases accuracy) has been offset by running several passes of the DFT on the same dataset (Westerweel *et al.*³³). Moreover, additional care has been taken to mitigate the issue due to the rotation and shear-induced stretching of the patterns typically produced by buoyancy convection in finite-size domains. These effects tend to broaden the intensity peak in the correlation matrix and deteriorate the result. Accordingly, the tracer displacement information at every pixel of the interrogation areas has been calculated via bilinear interpolation and accumulated in order to obtain a high accuracy after a few passes. Finally (post-processing stage), proper data interpolation has been implemented to replace the unavoidable missing vectors. In particular, PIVlab relies on a boundary value solver for interpolation, which prevents overshooting.³⁰

F. Vortex center position tracking

Additional insights into the considered dynamics have been gathered by tracking precisely the center of the main roll of buoyancy

nature established in the bulk of the liquid bridge. This has required the application of a different technique relying on a different visualization software, namely, “ImageJ.” Originally conceived to enable the investigation of dynamic processes in living cells at unprecedented spatial and temporal resolution (Chenouard *et al.*³⁴), this software allows accurate monitoring of the so-called “barycenter,” i.e., the center of mass of the pixels in a given “signal box” (the signal box is a user-defined area, i.e., a virtual cube centered on the tracked coordinates and encompassing the structure of interest).

III. RESULTS

Prior to expanding on the results, briefly recalling existing knowledge on RB convection is certainly beneficial. It is indeed instrumental in placing the present findings in a more general context.

As this field is so wide that an exhaustive review of the related origins and advances would be unrealistic, in order to keep this initial discussion concise and to the point, the salient topics touched upon in this preamble simply concern the specific findings and concepts effectively required for a better interpretation of the results presented later on. While apologizing to all whose work is not included in this account, we deliberately concentrate on the existing literature for cavities and enclosures exhibiting *axial symmetry*. Along these lines, it is worth recalling that this specific problem has been extensively studied through various approaches, including, but not limited to, experiments, linear stability analysis (LSA), and numerical simulations, which have led over the years to important insights and conclusions (the interested reader being referred, e.g., to Yamaguchi *et al.*,³⁵ Croquette *et al.*,^{36–39} Crespo Del Arco and Bontoux,⁴⁰ Crespo del Arco *et al.*,⁴¹ Neumann,⁴² Hardin and Sani,⁴³ Wagner *et al.*,⁴⁴ Touihri *et al.*,²⁸ Hof *et al.*,⁴⁵ Cheng *et al.*,⁴⁶ Leong,⁴⁷ and Boronska and Tuckermann⁴⁸).

Notably, as even a cursory perusal of these results would confirm almost immediately, remarkable differences exist with respect to the stress-free problem defined in Sec. II. In the case of a solid lateral wall (cylindrical enclosures), it is well known that the azimuthal wavenumber (m) of the flow depends on the aspect ratio ($A = \text{height}/\text{diameter} = L/D$). The thermal behavior of the cylindrical sidewall (adiabatic or conducting) can also have an impact. As an example, for the case of an adiabatic sidewall, the flow is axisymmetric for $A < 0.55$ ($m = 0$) and asymmetric for larger values of A ($m = 1$), while this transition occurs around $A = 0.72$ if the lateral wall is conductive (see, e.g., the experiments and numerical simulations for the case of water by Muller *et al.*¹). The critical Rayleigh number for the onset of flow from initially quiescent conditions also depends on the aspect ratio. The threshold value is $Ra_{cr} \cong 2000$ for the adiabatic case and $0.32 < A < 0.55$, and then the critical Rayleigh number increases with the aspect ratio ($Ra_{cr} \cong 3700$ for $A = 1$ and $Ra_{cr} \cong 2250$ for $A = 0.5$, with Ra_{cr} decreasing asymptotically toward the theoretical limit for an infinite layer, i.e., 1707 for $A \rightarrow 0$, Jeffreys⁴⁹).

A first important realization originating from this preliminary focused review of the properties of RB convection in the no-slip case is that, if there is one hallmark inherent to this type of flow in the *alternate configuration* considered here, i.e., the liquid bridge, it is its *inherent three-dimensional (3D) nature*. Unlike the cylindrical solid-wall configuration for which axisymmetric modes represent the preferred mode of convection at the onset in a certain interval of the aspect ratio, the present experiments clearly indicate that the flow emerging from the quiescent state for the liquid bridge is always three-dimensional. The related findings are discussed in Secs. III B–III D for the cases with

cylindrical ($S \cong 1$) and non-cylindrical ($S \neq 1$) volume, while Sec. III A is devoted to some propaedeutic concepts. As already stated in Sec. II B, all these results have been obtained using disks supporting the liquid bridge with a diameter of 5 mm.

A. Validation of the used experimental approach (comparison with LSA)

Given the peculiarity of the considered framework and the unconventional approach exploited to filter out the surface-tension-driven flow, this section deals with a necessary pre-requisite for an analysis like this, that is, the selection of a relevant process to verify the reliability of the overall theoretical-experimental architecture described in the earlier sections. After sifting through existing studies, trying to identify a benchmark, we could finally find such a relevant reference case in the study by Wanschura *et al.*,⁵⁰ namely, a linear stability analysis (LSA) concerning the onset of steady buoyancy flow from thermally diffusive and quiescent conditions in a perfectly cylindrical liquid bridge with adiabatic interface, heated from below and cooled from above.

We wish to remark that, despite its apparently innocuous nature and mathematical simplicity (at least in terms of boundary conditions), this problem features important “practical” pitfalls, requiring proper countermeasures.

First of all, the experimental detection of the critical threshold in this specific case poses challenges because, given the absence of fluid-motion-damping lateral walls, even a small departure from the horizontal orientation of the lower supporting disk can cause RB convection to be replaced by ILC, i.e., inclined buoyancy convection⁷ for which no threshold exists (fluid being put in motion regardless of the magnitude of the imposed temperature difference). An additional source of difficulty relates to the idealized adiabatic behavior of the free interface assumed by the aforementioned LSA. There is no possibility to thermally insulate the side boundary of a liquid bridge, which can, therefore, freely exchange heat with the surrounding environment. As already outlined in the introduction, this can lead to appreciable gradients of temperature in the radial direction, which can produce spurious fluid currents.

From a purely practical standpoint, we could control these issues through the consistent use of a digital inclinometer having a high accuracy and by heating and cooling symmetrically the liquid bridge in order to make its average temperature equal to that of the surrounding environment; moreover, we used a horizontal shield to damp fluid motion being induced by buoyant effects in the air surrounding the liquid bridge and mitigate accordingly heat exchange effects.

We wish also to highlight that this validation exercise was conducted for a specific value of the liquid bridge aspect ratio and related volume ratio (i.e., $A = 0.42$ and $S \cong 1$). Larger values of A and non-unit values of S had to be excluded as they were resulting in appreciable deformation of the interface and, again, departure from the ideal conditions considered in the LSA by Wanschura *et al.*⁵⁰

The outcomes of this approach are summarized in Fig. 7, which shows the maximum velocity inside the liquid bridge for different temperature differences. Such values were determined through *a posteriori* analysis of the videos recorded during the execution of the experiments. Using the DPIV technique described in Sec. II E, the effective distribution of velocity in the illuminated meridian plane (light cut)

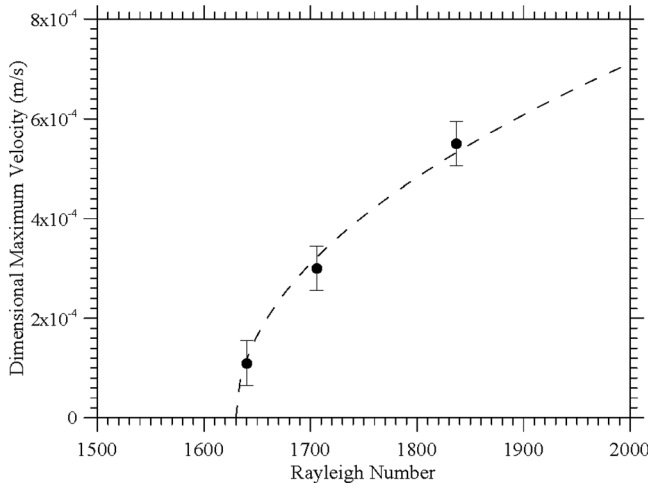


FIG. 7. Critical threshold detection ($A = 0.42$). Maximum velocity in the liquid bridge as a function of the Rayleigh number. The symbols denote effective measurements through DPIV, and dashed line indicates quadratic interpolation.

was found and the related *maximum* was extracted from the corresponding contour map.

The *critical Rayleigh number* has been estimated accordingly by extrapolating to zero the magnitude of the maximum velocity. As the reader will realize by comparing the obtained value ($Ra_{cr} \cong 1630$) with the LSA prediction⁵⁰ ($Ra_{cr(LSA)} \cong 1620$), there is excellent agreement. The present value is slightly larger than the theoretical counterpart, and we argue that this might be due to the unavoidable (although limited) departure of the interface from the idealized geometrical perfection

assumed in the LSA, or to the heat exchange with the environment occurring in proximity to the hot and cold disks (where the local temperature is appreciably larger or smaller than the average value).

B. Finite amplitude steady states for cylindrical liquid bridges

The present section is devoted to a more extended analysis of the results obtained for different liquid bridge aspect ratios in the case $S \cong 1$ over a range of the Rayleigh number spanning the interval from the onset of convection (primary instability) up to the appearance of unsteadiness (secondary instability, Hopf bifurcation).

In particular, the following procedure was implemented to gather such results. An increasing temperature difference (ΔT) was applied between the supporting disks. Each temperature difference was reached after approximately 20 s and then kept constant for 5 min (in order to allow the flow field to equilibrate) before starting to save the video. This was recorded for a couple of minutes only, longer experiments being made scarcely relevant by the evaporation phenomena and the corresponding variations (especially for very high ΔT) in the volume and shape of the liquid bridge. Overall, we ensured all the observations were made over time-periods for which the corresponding decrease in the volume was smaller than 5% and could be easily compensated through the addition of liquid (the flow velocity of the injected liquid, being significantly smaller than that of the convection present in the liquid bridge, the reader being referred to Gotoda *et al.*^{25,29} for additional details about this *modus operandi*).

The complete set of experiments conducted for different aspect ratios and temperature differences for which steady states were obtained are summarized together with the corresponding values of the Rayleigh number and the observed convective mode in Table II,

TABLE II. Experiments conducted for $S \cong 1$ and symmetric heating (steady states). Convective mode (number of rolls m) is reported as a function of the Rayleigh number for different values of the liquid bridge aspect ratio. The cases with more than a single value of m indicate states for which multiple solutions are possible.

$A = 0.3$																	
Ra	1913					2152					2391						
m	3					2, 3					3						
$A = 0.42$																	
Ra	1574	1640	1706	1837	1968	2099	2231	2362	2493	2624	3280	3936	4592	5248			
m	2	2	2	2	2	2	2	2	2	2	2	2	2	2			
$A = 0.6$																	
Ra	1721	1913	2295	2678	3060	3825	4208	4590	5738	7268	7651	9653	13 388	19 126			
m	1, 2	2	1	2	2	2	2	2	1, 2	1	1	1	1	1			
$A = 0.7$																	
Ra	9112			12 149			15 186			18 223			21 260			24 298	
m	1			1			1			1			1				
$A = 0.9$																	
Ra	25 821				32 276				38 731				45 186				51 641
m	1				1				1				1				

16 May 2024 12:37:44

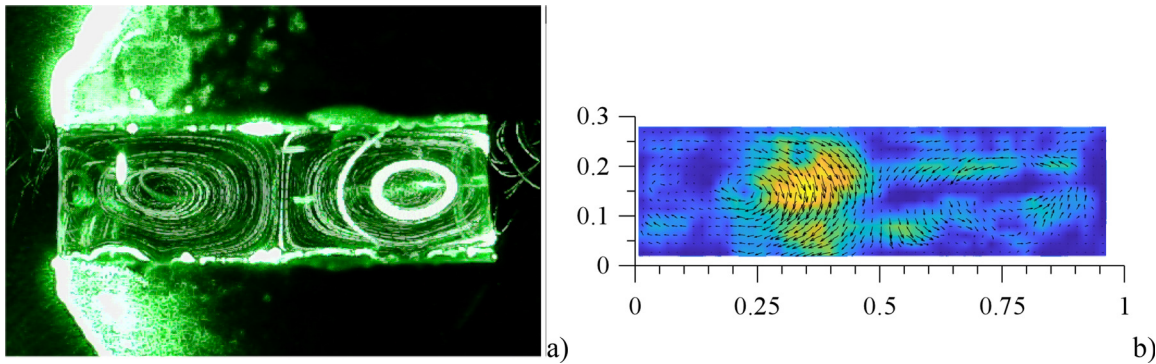


FIG. 8. Two-steady-roll state in liquid bridge with aspect ratio $A = 0.3$, $S \cong 1$, $T_{cold} \cong 0^\circ\text{C}$, $\Delta T = 45\text{ K}$ ($Ra = 2152$, $Bo \cong 0.3$): (a) long-exposure picture (over 12.5 s) and (b) PIV vector plot. Velocity magnitude: yellow color: $3.5 \times 10^{-4}\text{ m/s}$, blue color, $5 \times 10^{-5}\text{ m/s}$. The coordinates have been scaled by the liquid bridge diameter.

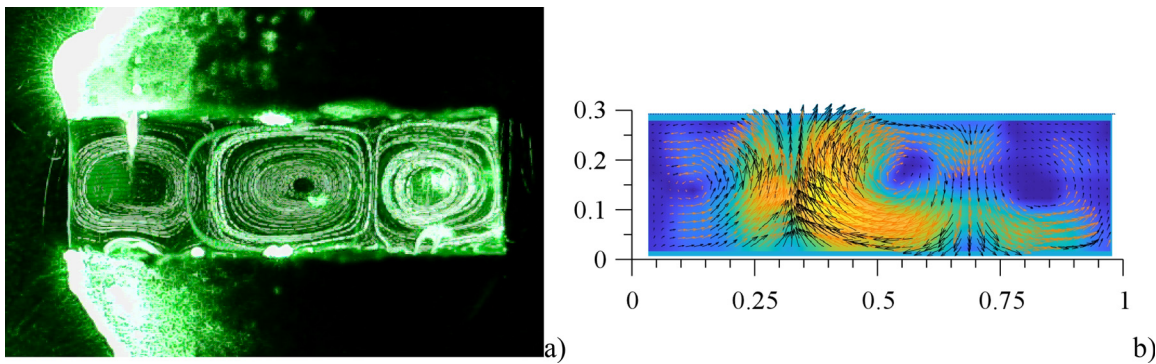


FIG. 9. Three-steady-roll state in liquid bridge with aspect ratio $A = 0.3$, $S \cong 1$, $T_{cold} \cong 0^\circ\text{C}$, $\Delta T = 45\text{ K}$ ($Ra = 2152$, $Bo \cong 0.3$): (a) long-exposure picture (over 12.5 s) and (b) PIV vector plot. Velocity magnitude: yellow color: $4.5 \times 10^{-4}\text{ m/s}$, blue color, $5 \times 10^{-5}\text{ m/s}$. The coordinates have been scaled by the liquid bridge diameter.

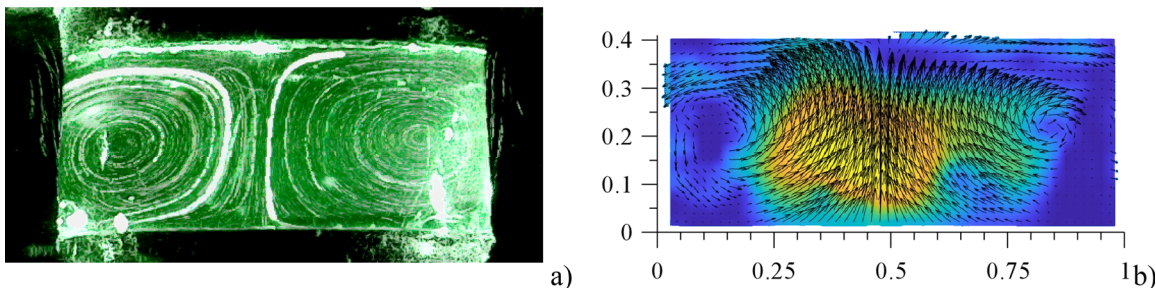


FIG. 10. Two-steady-roll state in liquid bridge with aspect ratio $A = 0.42$, $S \cong 1$, $T_{cold} \cong 0^\circ\text{C}$, $\Delta T = 40\text{ K}$ ($Ra = 4540$, $Bo \cong 0.54$): (a) long-exposure picture (over 6.5 s) and (b) PIV vector plot. Velocity magnitude: yellow color: $6 \times 10^{-4}\text{ m/s}$, blue color, $1 \times 10^{-4}\text{ m/s}$. The coordinates have been scaled by the liquid bridge diameter.

the reader being also referred to the examples shown in Figs. 8–12. (Note: In some cases, the PIV was not able to capture/reconstruct properly the velocity in proximity to the domain boundaries; those thin portions have not been included in the figures.)

As made evident by this table, specific disturbance modes are selected out of the full spectrum of disturbances over certain ranges of the aspect ratio and they persist as the preferred spatial mode of convection over relatively extended intervals of the Rayleigh number. In agreement with the predictions of the aforementioned linear stability

analysis,⁵⁰ we could observe no axisymmetric states of convection over the entire space of parameters investigated, which may be regarded as an important distinguishing mark with respect to the companion situation with solid lateral boundary (where, as illustrated at the beginning of Sec. III, the axisymmetric mode is allowed for $A < 0.55$). Although the two vortices shown in Figs. 10 and 12 look symmetric with respect to the liquid bridge axis, they represent a couple of “parallel” rolls. The absence of the axisymmetric mode in all cases considered has been verified through progressive rotation (in the horizontal plane) of the laser

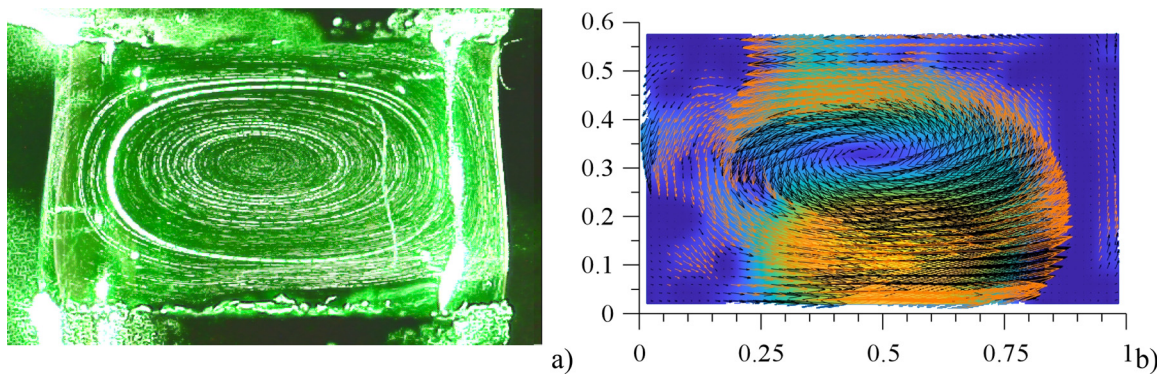


FIG. 11. Single steady roll in the (symmetry) meridian plane ($m = 1$) of liquid bridge with aspect ratio $A = 0.6$, $S \cong 1$, $T_{\text{cold}} \cong 0^\circ\text{C}$, $\Delta T = 15\text{ K}$ ($Ra \cong 5740$, $Bo \cong 1.2$): (a) long-exposure picture (over 12.5 s) and (b) PIV vector plot. Velocity magnitude: yellow color: $9 \times 10^{-4}\text{ m/s}$, blue color, $1 \times 10^{-4}\text{ m/s}$. The coordinates have been scaled by the liquid bridge diameter.

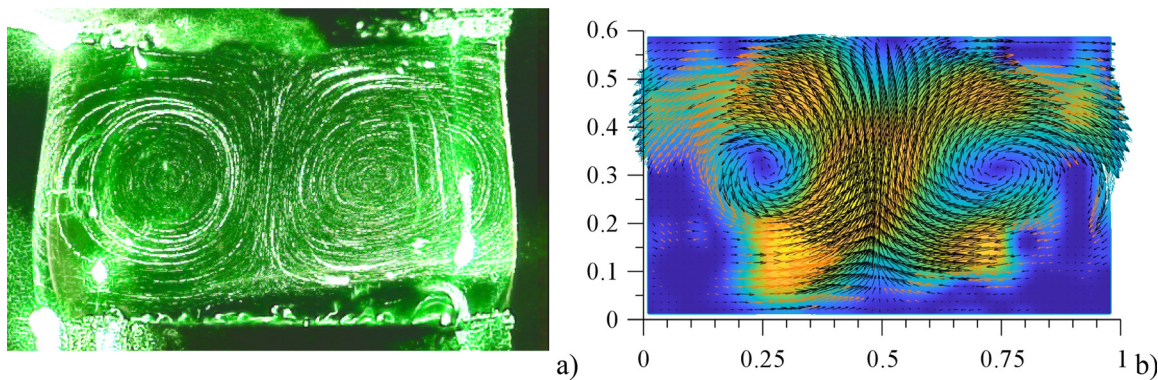


FIG. 12. Two-steady-roll state in liquid bridge with aspect ratio $A = 0.6$, $S \cong 1$, $T_{\text{cold}} \cong 0^\circ\text{C}$, $\Delta T = 15\text{ K}$ ($Ra \cong 5740$, $Bo \cong 1.2$): (a) long-exposure picture (over 12.5 s) and (b) PIV vector plot. Velocity magnitude: yellow color: $5 \times 10^{-4}\text{ m/s}$, blue color, $5 \times 10^{-5}\text{ m/s}$. The coordinates have been scaled by the liquid bridge diameter.

beam and corresponding rotation of the axis of the camera used to visualize the flow in a section perpendicular to the laser cut. Such a rotation has been observed to produce always appreciable changes in the visualized pattern.

As an example, the pattern shown in Fig. 8 has been obtained for $A = 0.3$ by progressively rotating the observation plane (that is the light sheet and the perpendicular camera) up to visualize two apparently symmetric rolls. For a *perpendicular observation direction* (i.e., rotated by 90° with respect to that by which Fig. 8 has been produced), a trivial convective pattern was obtained with no recognizable rolls, i.e., all streamlines were vertical and parallel (not shown), simply reflecting the displacement of tracers in the vertical (upward or downward) direction. Accordingly, the two counter-rotating vortices seen in Fig. 8 should be interpreted as the intersection of two parallel rolls extended in a direction perpendicular to the light cut with the light cut itself. A similar concept also applies to all the other multi-cellular configurations shown in Figs. 9–12. The visualized patterns always correspond to the intersection of a set of rolls (Figs. 9, 10, and 12) or a single roll (Fig. 11) of RB nature with the visualization (illuminated) plane. The roll number (m) essentially depends on the aspect ratio and (yet in

agreement with the general properties of RB convection) tends to become smaller as the aspect ratio is increased.^{35–48}

Another key remark concerns the existence of *multiple solutions*, i.e., the ability of the considered system to select (in an apparently random way) different steady modes of convection for a fixed aspect ratio and Rayleigh number (see Table II). As demonstrated by other studies based on numerical simulations,^{8–10,45,47,48} these alternate states can be accessed through relevant changes in the initial conditions because they exist in the space of phases as independent solutions with disjoint basins of attraction (Yao,⁵¹ Kengne *et al.*⁵²). In particular, we could observe this feature of RB convection when conducting the experiments for $A = 0.3$ (Figs. 8 and 9) and $A = 0.6$ (Figs. 11 and 12). Notably, for these specific aspect ratios, the liquid bridge has displayed the fascinating ability to jump from a solution with a given number or rolls to an alternate state (with different m) and vice versa if subjected to a finite-amplitude external disturbance or stimulus, namely, disruption of the existing flow by means of a solid obstacle (a small stick inserted laterally in the liquid bridge and used to remix the fluid). The structure of the two alternate 3D solutions for $A = 0.3$ is sketched in Fig. 13. We could not detect similar behaviors for the other considered

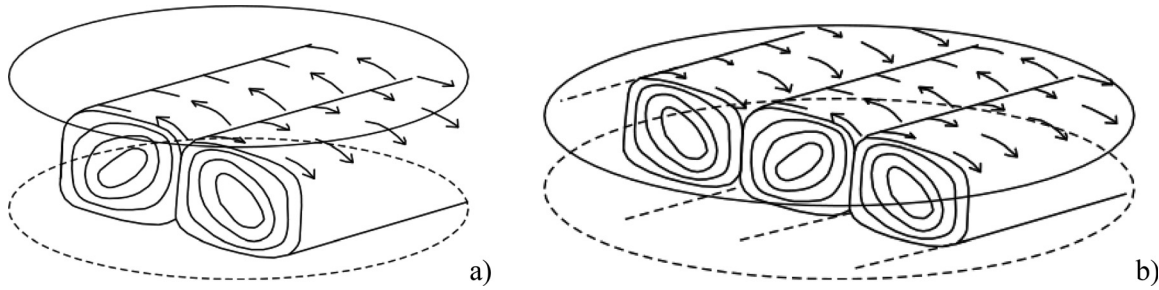


FIG. 13. Sketch of the $m = 2$ (a) and $m = 3$ (b) alternate solutions for $A = 0.3$.

aspect ratios $A = 0.42, 0.7,$ and 0.9 (at least not in the accessible interval of values of the Rayleigh number).

C. Rocking motion and higher modes of convection

Continuing with the description of the convective states that emerge on increasing the applied temperature difference, it is worth pointing out that, in line with expectations (i.e., by analogy with the known behavior of RB convection in cylindrical enclosures⁷), well-defined secondary modes of convection can be produced also in the liquid bridge case.

Before starting to deal with this aspect, we wish to remark that the results discussed in Sec. III B were obtained paying special attention to the need to heat and cool the liquid bridge symmetrically (in order to minimize the heat exchange with the surrounding environment). However, we could no longer implement symmetric heating for larger temperature differences, given the inability of the thermal control system to produce temperatures on the upper disks smaller than $\cong 0^\circ\text{C}$ (smaller values being out of reach also for the well-known transition to the ice state occurring in water for such temperatures).

Accordingly, for this set of temperature differences, the average temperature of the liquid bridge ($T_{avg} = T_{cold} + T_{hot})/2$ was larger than the ambient temperature (T_{air}); therefore, some heat exchange with the external ambient was taking place.

For the sake of completeness, in the following, we conveniently estimate this effect through the average Biot number and related analytical expressions. In particular, we refer to the so-called Senglebe's relationship reported by Boetger⁵³ by which the Biot number can be determined as a function of the air Prandtl and Grashof numbers as follows:

$$Bi = \frac{hL}{\lambda_{liquid}}, \tag{6}$$

where the liquid thermal conductivity λ_{liquid} is evaluated at the average T_{avg} and the convective heat exchange coefficient h is computed as

$$h = \frac{2\lambda_{air}}{\varphi D} \left\{ 1 - \frac{0.102}{\varphi (Gr_{air} Pr_{air})^{1/4}} \left[\sqrt{\left(1 + \frac{\varphi (Gr_{air} Pr_{air})^{1/4}}{0.130} \right)} - 1 \right] \right\}, \tag{7a}$$

where

$$\varphi = \ln \left[1 + \frac{L}{D} \frac{3.34}{(Gr_{air} Pr_{air})^{1/4}} \right], \tag{7b}$$

$$Pr_{air} = \frac{\nu_{air}}{\alpha_{air}}, \quad Gr_{air} = \frac{g\beta_{air}(T_{avg} - T_{air})(L^3)}{\nu_{air}^2}. \tag{7c}$$

Here, β_{air} , ν_{air} and α_{air} are the thermal expansion coefficient, kinematic viscosity, and thermal diffusivity of air evaluated at a reference representative temperature, that is, $T_{ref} = (T_{avg} + T_{air})/2$.

It is also worth pointing out that, in addition to the heat exchange of a purely convective nature quantified through Eq. (7a), water evaporation could also lead to local cooling along the free liquid–gas interface. As this effect was limited to the portion of the interface where the temperature was larger than the ambient temperature, that is, in proximity to the bottom hot disk, however, we assume it to be negligible in comparison to the large-scale effect (affecting the entire free surface) produced by external convection.

The most effective way to undertake a description of all the related experimental findings is to start from the remark that, for all cases with $A = 0.6$ and $A = 0.7$ for which $m = 1$ (the estimated Biot number being generally smaller than 0.1), we could observe flow oscillations essentially manifesting themselves as a periodic displacement in the position of the core of the main vortex visible in the light cut plane (the symmetry plane shown in Fig. 14).

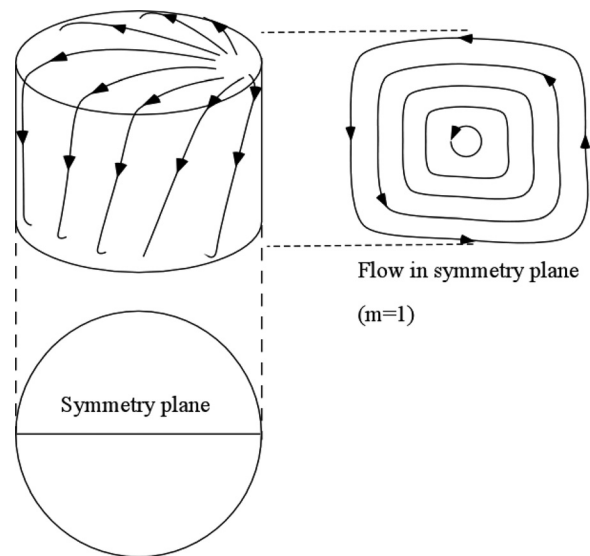


FIG. 14. Structure of RB flow in the liquid bridge for $m = 1$.

16 May 2024 12:37:44

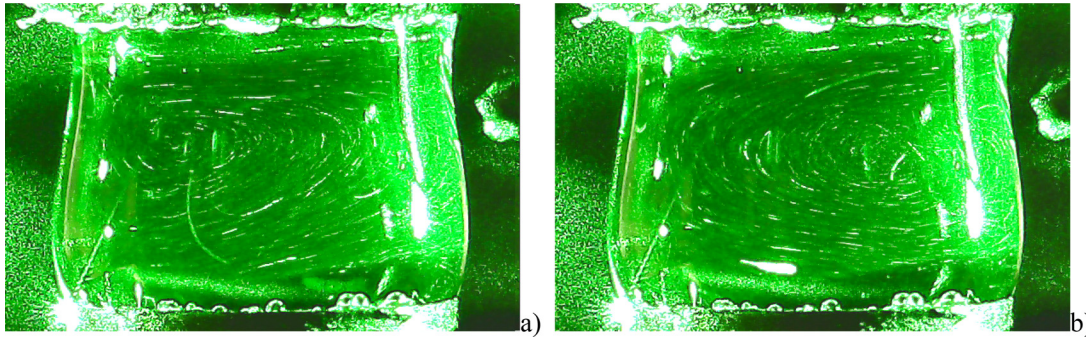


FIG. 15. Snapshots of oscillatory buoyancy flow in a liquid bridge with aspect ratio $A = 0.7$, $S \cong 1$, $T_{cold} = 5^\circ\text{C}$, $\Delta T = 50\text{ K}$ ($Ra = 30\,440$, $Bo = 1.65$, $Bi \cong 7.5 \times 10^{-2}$): (a) $t = t_0$ and (b) $t = t_0 + \tau/2$ (dimensional period $\tau = 2.364\text{ s}$, corresponding non-dimensional frequency $f = 36.22$).

It is also worth highlighting that, although minute (unavoidable) departures from a perfectly axisymmetric shape of the liquid bridge were noted in some circumstances (see Fig. 15), the emerging asymmetrical flow structure did not depend on them. In this regard, we wish to recall that all the experiments described in the present work were executed two or even more times to verify repeatability and independence from initial, environmental, and other conditions.

In particular, the flow visible in Fig. 15 ($A = 0.7$, $Ra = 30\,440$) can essentially be regarded as a single roll encapsulated inside the liquid bridge. The departures from the classical two-dimensional vortex, which would be produced in an infinite layer, are simply due to the adjustments that its external shape must accommodate in order to fit the cylindrical symmetry of the liquid bridge. Notably, this results in a well-defined plane of symmetry, ideally splitting the liquid bridge into two identical halves (see again Fig. 12). This is the plane where the maximum velocity occurs, and as already explained in Sec. III B, we had to rotate consistently the light cut in order to uniquely identify it in the experiments, (by changing the position of the laser source and of the camera used to record images accordingly) up to obtain a well-centered roll occupying the entire horizontal extension of the liquid bridge.

Interestingly, Fig. 15 also reveals the presence of small “bubbles” close to the bottom (hot) disk, for which we provide in the following a short excursus for the sake of completeness. Obviously, the temperature of the bottom disk was larger than the ambient temperature. Although it was not sufficiently large to cause boiling phenomena (requiring at least 100°C), however, we argue that it could cause localized evaporation. The present experiments showed indeed that, owing to such localized evaporation phenomena, small bubbles of vapor were created and trapped at the intersection between the disk edge and the free liquid–air interface. Unfortunately, we are not in a condition to provide additional details about this fascinating phenomenon. As shown by various analyses existing on this specific subject (see, e.g., Song and Fan⁵⁴), the dynamics of liquid–vapor heterogeneous phase change phenomena in proximity to a heated solid surface can be very complex, and the exact molecular mechanisms underlying these experimental observations remain largely unclear. Similarly, quantifying the effects of such bubbles on the fluid flow is extremely difficult. Given the random nucleation positions of such bubbles and the aforementioned repeatability of the experiments for a given aspect ratio and temperature difference, however, we infer that their effect can be somehow considered negligible.

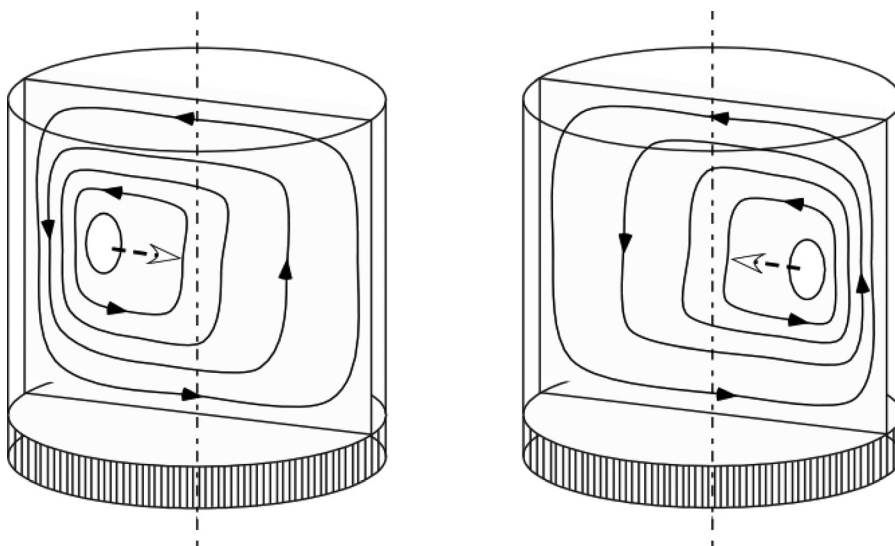


FIG. 16. Sketch of oscillatory behavior in the case $m = 1$. The white arrow indicates the time-periodic displacement of the vortex core in the horizontal direction.

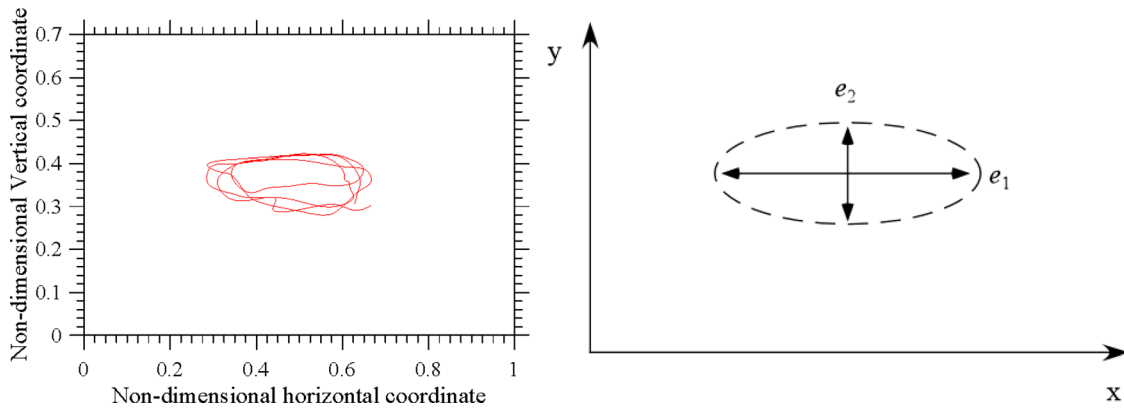


FIG. 17. (a) Vortex center trajectory in the meridian plane for the following conditions: $A = 0.7$, $S \cong 1$, $Bo \cong 1.65$, $T_{cold} = 5^\circ\text{C}$, $\Delta T = 46\text{ K}$, $Ra = 28\,000$, $Bi \cong 7.1 \times 10^{-2}$, monitored time $\cong 7.5\text{ s}$, period of oscillation $\tau = 2.46\text{ s}$ (corresponding to a non-dimensional frequency $f \cong 34.7$). The coordinates have been scaled by the liquid bridge diameter, the monitored time is $\cong 10\text{ s}$. (b) Sketch of the approximately elliptical trajectory path.

For the convenience of the reader, a sketch of the flow established in the bulk of the liquid bridge is illustrated in Fig. 16. Put simply, for values of Ra slightly larger than the first value for which time-dependence is detected (hereafter referred to as Ra_{cr2}), the periodic displacement of the vortex essentially results in a continuous back and forth motion of its center in the horizontal direction; nevertheless, no change occurs in the roll direction of circulation (which retains in time its “original” clockwise or counterclockwise orientation, depending on the initial conditions).

Following up on the previous point, Fig. 17 shows the trajectory described in space by the center of the roll, tracked using the algorithm described in Sec. II E.

A first key observation stemming from Fig. 17(a) concerns the realization that, not too far (in terms of applied ΔT) from the onset of unsteadiness, the roll-center motion in horizontal direction [quantitatively represented by the corresponding amplitude e_1 , see Fig. 17(b)] dominates over the corresponding unsteady displacement in the vertical direction (i.e., $e_1 > e_2$, which explains why the trajectory “loop” displays a relatively flattened shape). On a separate note, it is worth recalling that this circuit in the xy plane obviously reflects the existence of a “limit cycle” in the phase space, i.e., a time-periodic solution, which, in turn, can be associated with a well-defined frequency (still pursuing a geometric analogy between the limit cycle in the phase space and the corresponding circuit in the meridian plane, this frequency might be seen or interpreted as a measure of the rate at which the vortex center travels along this closed path).

Even more importantly, these repetitive trajectories are instructive as they contain quantitative information about the *finite-amplitude nature* of these states. Most conveniently, here, we assume this representative amplitude to be just the major axis e_1 of the loop, as this specific choice leads to another remarkable outcome, that is, the possibility to characterize these behaviors in terms of two parameters only, namely, the flow frequency and the *ad hoc* defined parameter e_1 itself.

The outcomes of this “spatial” way of thinking can be appreciated (yet for $A = 0.7$) by taking a look at Fig. 18 from which the evolution of the parameter e_1 in a relatively small neighborhood of the instability threshold can be gathered (the reader being referred to the portion of the plot delimited by the vertical axis on the left and the vertical dashed

line on the right, i.e., the interval $24\,000 < Ra < 32\,000$). In this range, e_1 naturally tends to zero for decreasing values of the imposed temperature difference (Rayleigh number), or vice versa, it grows on increasing Ra until a “saturated” regime is entered for $Ra > 32\,000$ where e_1 does not depend much on the considered conditions (a small non-monotonic behavior can be seen there; it first decreases and then tends to grow again as the Rayleigh number is further increased).

The transition from steady to time-periodic flow is obviously just a first step along the evolutionary path leading the system to a more involved state. In the following, we show that an understanding of the unsteady states for $Ra > 32\,000$ can still be provided through a spatially

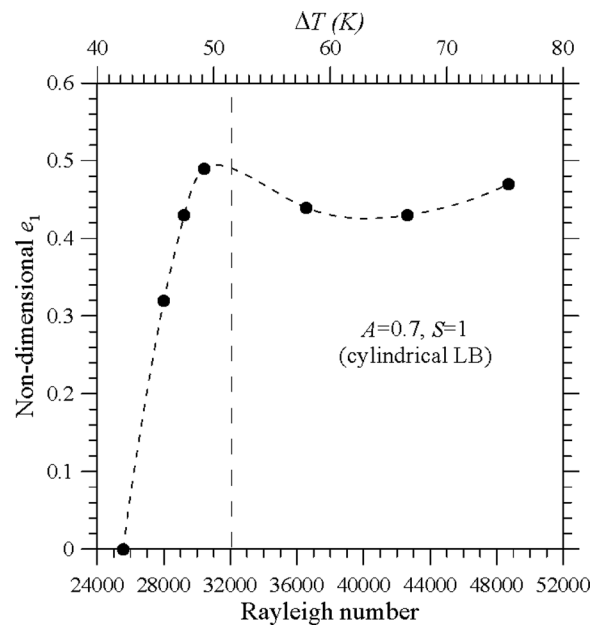


FIG. 18. Non-dimensional major axis (e_1) of trajectory loop as a function of the Rayleigh number for $A = 0.7$, $Bi \leq 0.1$, and $S \cong 1$ ($Ra_{cr2} \cong 25\,570$). The spline is used to guide the eye.

16 May 2024 12:37:44

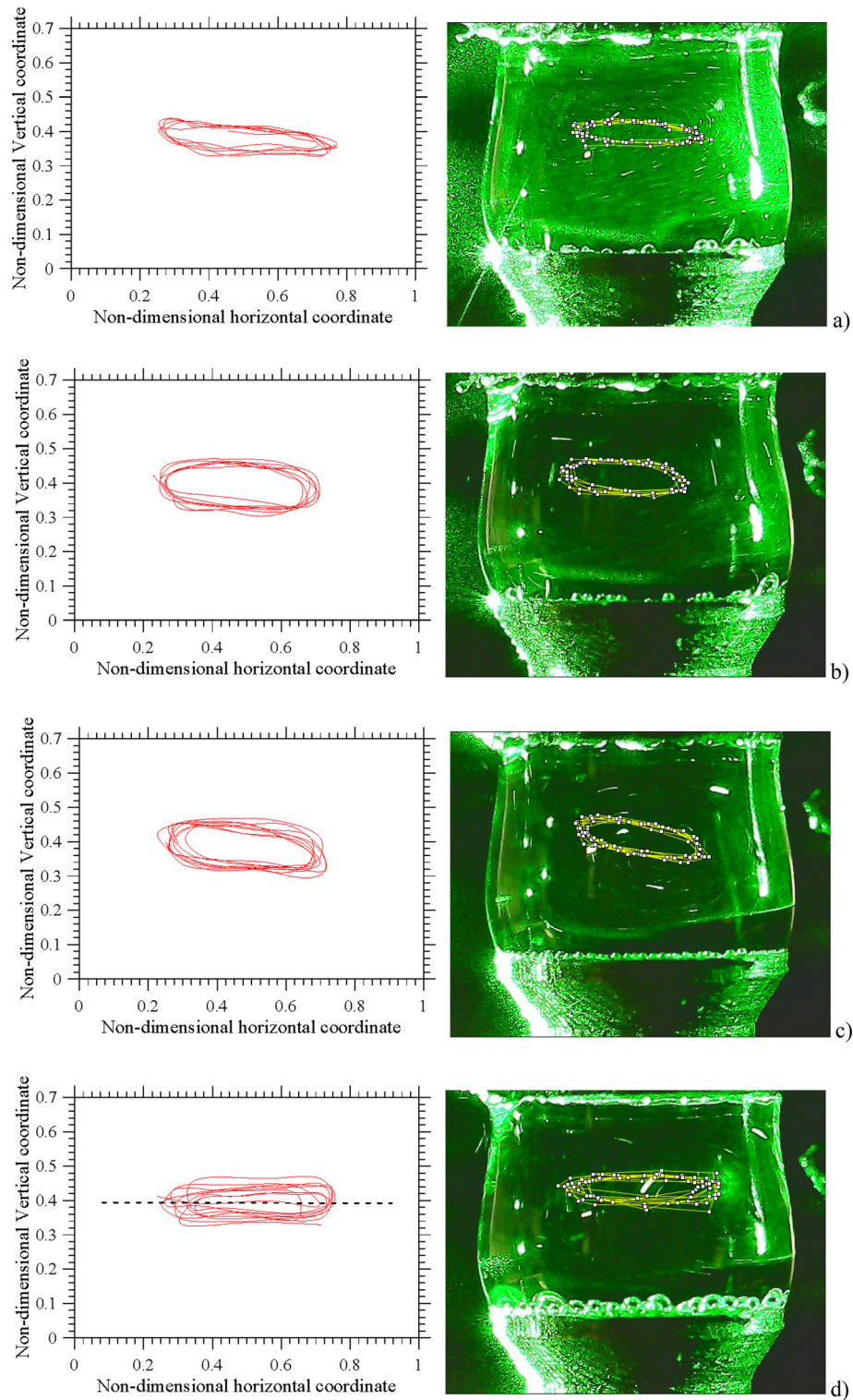


FIG. 19. Vortex center trajectory in the meridian plane (aspect ratio $A = 0.7$, $S \cong 1$, $Bo \cong 1.65$, T_{cold} fixed to 5°C): (a) $\Delta T = 50\text{ K}$ ($Ra = 30\,440$, $\varepsilon \cong 0.19$, $Bi \cong 7.5 \times 10^{-2}$); (b) $\Delta T = 60\text{ K}$ ($Ra = 36\,530$, $\varepsilon \cong 0.43$, $Bi \cong 8.1 \times 10^{-2}$); (c) $\Delta T = 70\text{ K}$ ($Ra = 42\,620$, $\varepsilon \cong 0.65$, $Bi \cong 8.6 \times 10^{-2}$); and (d) $\Delta T = 80\text{ K}$ ($Ra = 48\,700$, $\varepsilon \cong 0.9$, $Bi \cong 9 \times 10^{-2}$) (the coordinates have been scaled by the liquid bridge diameter, the monitored time is $\cong 10\text{ s}$).

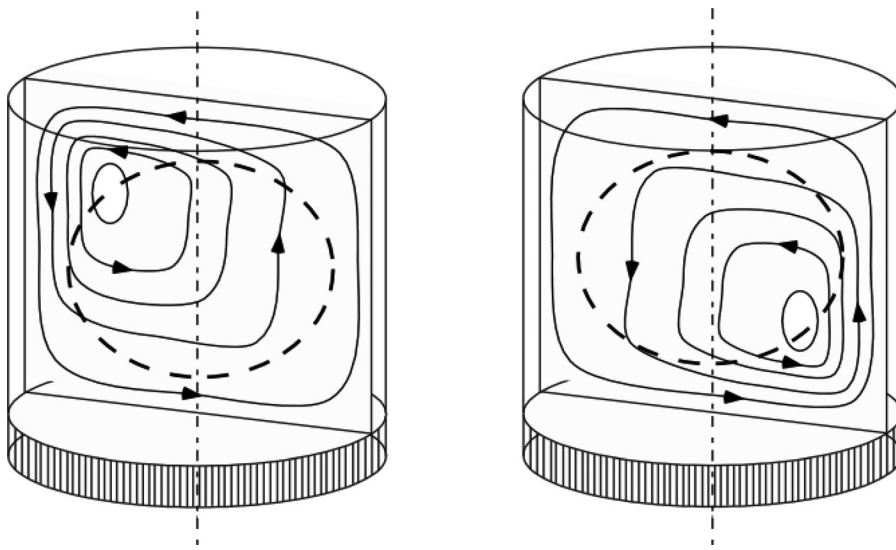


FIG. 20. Sketch of oscillatory behavior with periodic up-and-down migration of the roll center in the case $m = 1$. The dashed line indicates the closed path described by the vortex core over one period of oscillation.

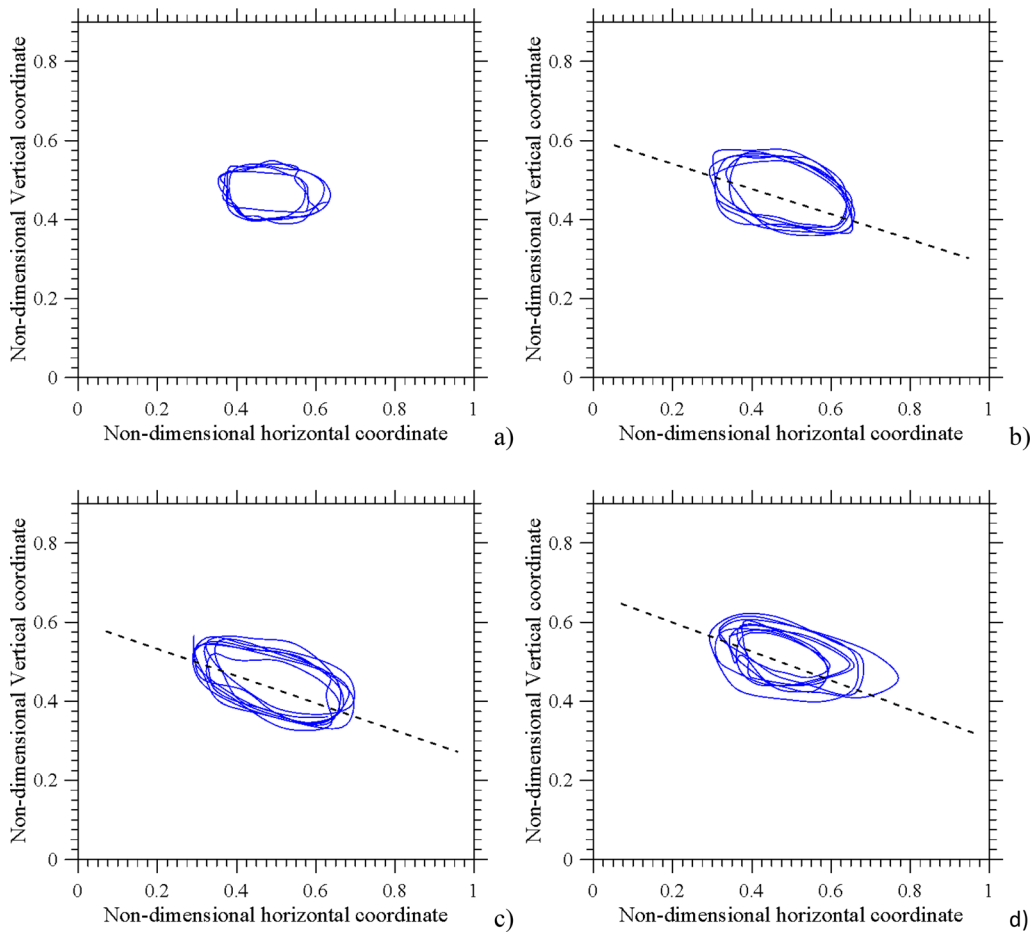


FIG. 21. Vortex center trajectory in the meridian plane (aspect ratio $A = 0.9$, $S \cong 1$, $Bo \cong 2.73$, T_{cold} fixed to 5°C): (a) $\Delta T = 50\text{ K}$ ($Ra = 64\,700$, $\varepsilon \cong 0.11$, $Bi \cong 9.3 \times 10^{-2}$); (b) $\Delta T = 60\text{ K}$ ($Ra = 77\,640$, $\varepsilon \cong 0.33$, $Bi \cong 0.1$); (c) $\Delta T = 70\text{ K}$ ($Ra = 90\,580$, $\varepsilon \cong 0.56$, $Bi \cong 0.107$); and (d) $\Delta T = 80\text{ K}$ ($Ra = 103\,520$, $\varepsilon \cong 0.78$, $Bi \cong 0.11$). The coordinates have been scaled by the liquid bridge diameter, the monitored time is $\cong 10\text{ s}$.

16 May 2024 12:37:44

based perspective, i.e., an analysis of the additional degrees of freedom, which are progressively activated in the dominant vortex as the temperature difference is increased (Fig. 19).

The significance of this figure primarily resides in its ability to make evident that, on increasing the distance from the onset of unsteadiness, which we define as

$$\varepsilon = \frac{Ra - Ra_{cr2}}{Ra_{cr2}}, \quad (8)$$

an additional spatial degree of freedom is enabled for $\varepsilon > 0.25$ ($Ra > 32\,000$), i.e., a periodic up-and-down migration of the roll center is also noticeable in addition to the aforementioned essentially horizontal (rhythmic) drift (e_2 grows significantly with respect to the limited values it was displaying for smaller values of the imposed temperature difference, this being very evident in Figs. 19(b) and 19(c), the reader being also referred to the sketch shown in Fig. 20).

Interestingly, the activation of this additional degree of freedom (e_2) is initially associated with a corresponding decrease in the value of e_1 , i.e., the extension of the major axis decreases in conjunction with the observed growth of e_2 . However, the rising trend of e_2 with Ra is

recovered at a later stage ($Ra > 40\,000$). Finally, for relatively high values of the Rayleigh number [$Ra \cong 48\,000$, see Fig. 19(d)], the trajectory loses the well-defined repetitive behavior visible for smaller temperature differences. Yet building on the parallelism defined before between the physical and phase spaces, we wish to remark that, just as the single (repetitive) loop obtained for relatively small values of the imposed ΔT can be considered representative of a well-defined limit cycle in the space of phases, this more involved trajectory should be seen a realization in space of a corresponding overarching “attractor” (yet existing in the phase space), i.e., an object having as many dimensions as the number of degrees of freedom of the system (Bergè *et al.*⁵⁵).

The lack of a perfectly repetitive behavior is clearly witnessed by the tendency of the vortex center to occupy in time all the positions encapsulated into a region of limited extension, rather than being constrained to travel continuously (just like a train on a rail) along a well-defined elliptic loop with fixed minor and major axes. We ascribe this behavior to a modulation in time of the axes e_1 and e_2 . This is essentially the reason why the internal part of the vortex core residence area in Fig. 19(d), which was previously clear (i.e., never touched by the vortex center), is now colored.

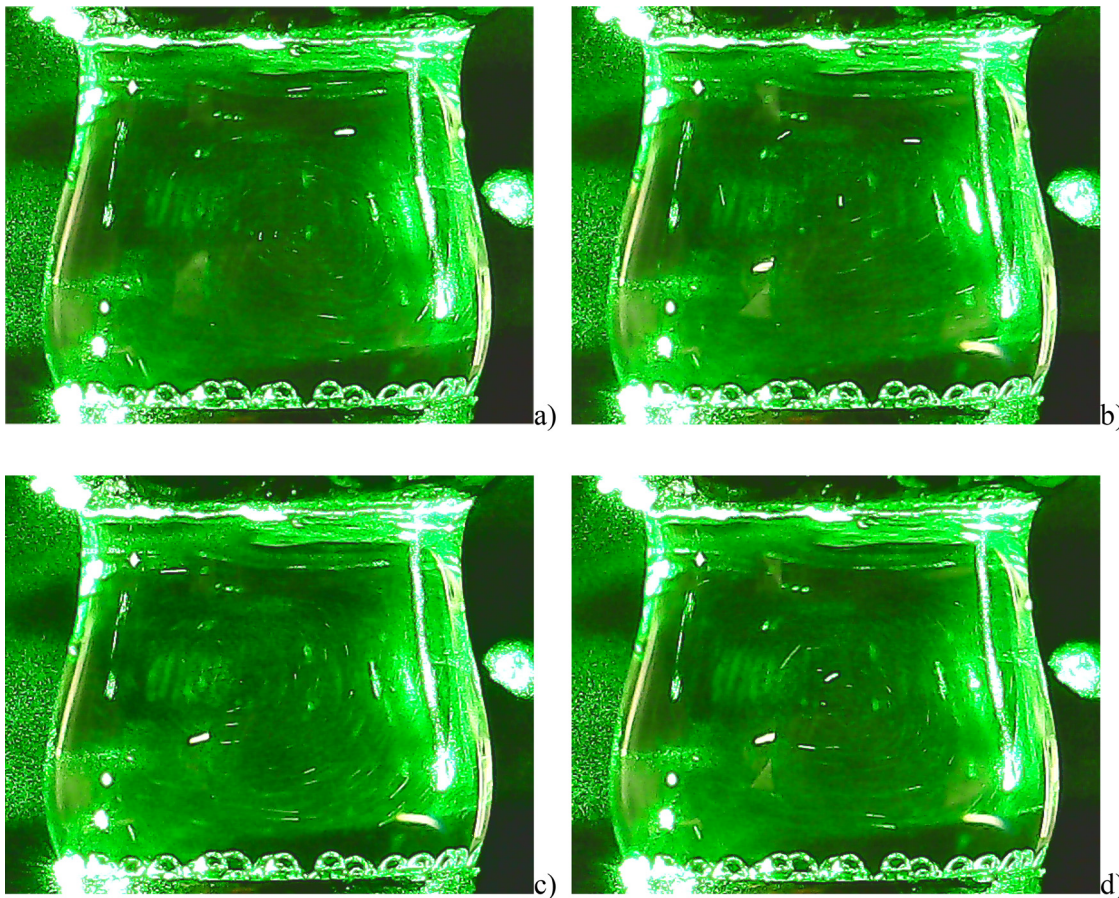


FIG. 22. Snapshots of oscillatory buoyancy flow in a liquid bridge with aspect ratio $A = 0.9$, $S \cong 1$, $Bo \cong 2.73$, $T_{cold} = 5^\circ\text{C}$, $\Delta T = 60\text{ K}$, $Ra = 77\,640$, $\varepsilon \cong 0.33$, $Bi \cong 0.1$: (a) $t = t_0$, (b) $t = t_0 + \tau/4$, (c) $t = t_0 + \tau/2$, and (d) $t = t_0 + 3\tau/4$ (dimensional period $\tau = 2.018\text{ s}$, corresponding non-dimensional frequency $f = 70.15$). The vortex center is moving in the counterclockwise direction.

Figure 19 is naturally complemented by the corresponding dynamics obtained for $A = 0.9$ shown in Fig. 21.

Comparison of Figs. 19 and 21 indicates that, in addition to causing an increase in the critical Rayleigh number for the onset of unsteadiness ($Ra_{cr2} \cong 5.8 \times 10^4$, $\Delta T \cong 45$ K for $A = 0.9$), a larger aspect ratio can also have an impact on the prevailing spatiotemporal behavior. For $A = 0.9$, the loop major axis e_1 undergoes a shrinkage with respect to the equivalent conditions for $A = 0.7$ (in terms of distance from the onset of time-dependence, i.e., for a similar value of the parameter ϵ), and the key to understanding the results lies in considering that the horizontal extension of the roll is generally comparable to its axial extension, which obviously leaves more room to the aforementioned horizontal rhythmic displacement in the cases where $D \gg L$ (i.e., the smaller the aspect ratio, the larger the ability of the roll to change its horizontal position periodically).

A larger aspect ratio also has another interesting consequence. Figure 21, which shows selected examples of the dynamics for increasing values of ΔT , also reveals that the vortex center in this case displays essentially a diagonal motion, as witnessed by the inclination of the dashed line included in each panel. This behavior is also appreciable in Fig. 22.

Additional insights finally follow from Fig. 23, where we have reported Ra_{cr2} vs the aspect ratio and summarized available data about

the prevailing flow frequency as a function of the Rayleigh number. We wish to remark that the frequency has been put in non-dimensional form using the thermal diffusion time L^2/α and that we could not find oscillations in the $A = 0.42$ case in the accessible interval of temperature differences (the evaluation of the second critical Rayleigh number being, therefore, out of reach for this case).

D. Non-cylindrical liquid bridges

The results presented in this section finally deal with circumstances where the volume held between the disks is intentionally made larger ($S > 1$) or smaller ($S < 1$) than that of an equivalent cylinder with the same base and height, the former (latter) condition corresponding to convex (concave) liquid bridges. The final objective is an assessment of the influential role played by the S additional geometrical parameter. Although a vast literature dealing with this specific aspect exists in the case of liquid bridges supporting Marangoni flow (Hu *et al.*,^{56,57} Hu and Tang,⁵⁸ and Hirata *et al.*^{59–61}), there seems to be no (experimental/theoretical/numerical) results at all for RB convection in configurations with stress free and deformed (non-straight) lateral boundary.

For simplicity, we concentrate on the intermediate value of the aspect ratio, i.e., $A = 0.7$ for which (unlike the case $A = 0.6$) we found

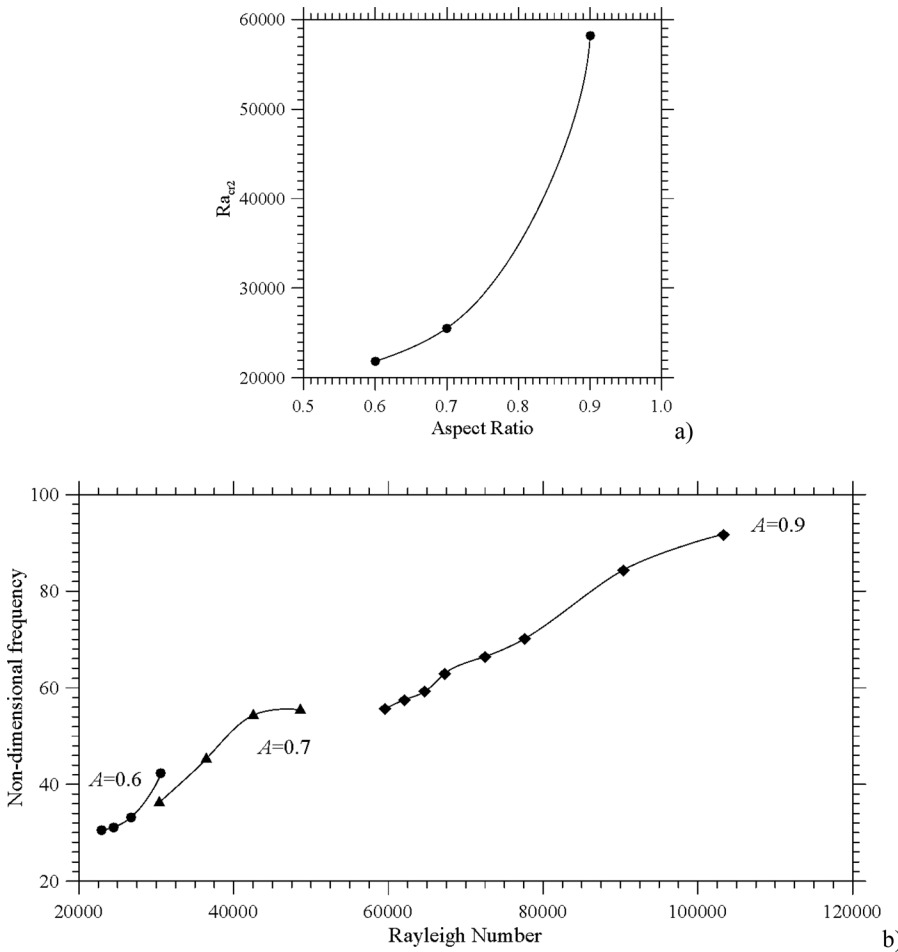


FIG. 23. (a) Ra_{cr2} as a function of the aspect ratio. (b) Non-dimensional oscillation frequency as a function of the Rayleigh number for different values of the aspect ratio [$S \cong 1$, $Bi \leq O(10^{-1})$]. The frequency has been made non-dimensional using the thermal diffusion time based on the liquid bridge height (L^2/α). The splines are used to guide the eye.

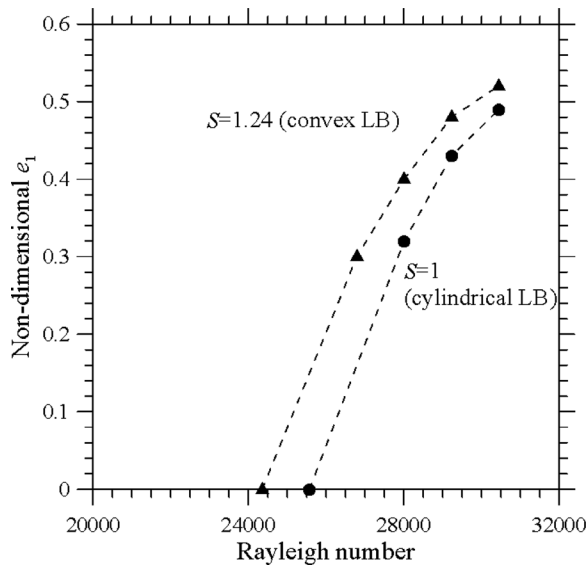


FIG. 24. Non-dimensional major axis (e_1) of trajectory loop as a function of the Rayleigh number for $A = 0.7$, $S \cong 1.24$, and $Bo \cong 1.65$. The splines are used to guide the eye.

no multiple solutions and the aspect ratio was still sufficiently small not to cause excessive interface deformation due to gravitational effects (unlike the case $A = 0.9$).

A first sub-set of instructive experimental findings for this case are presented in Fig. 24, which also includes the experiments already described in Sec. III C for $S = 1$ in a certain neighborhood of the Hopf bifurcation point, i.e., $Ra > Ra_{cr2}$.

As implicitly revealed by a comparative assessment of the two branches for $S \cong 1$ and $S \cong 1.24$, tracking the system in terms of the e_1 parameter still leads to meaningful results as it makes evident that a

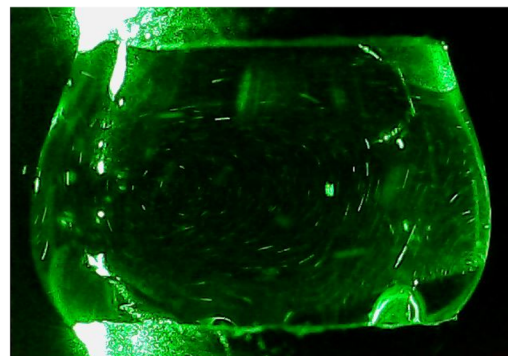
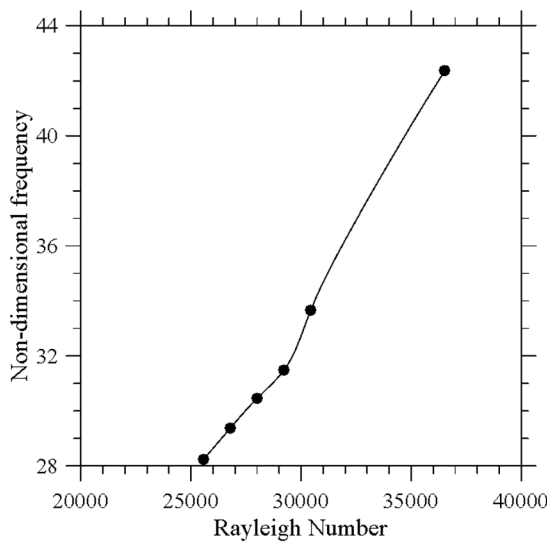
larger volume can destabilize the flow, i.e., cause a decrease in the value of the Rayleigh number required for the onset of time-dependence ($Ra_{cr2} \cong 24\,350$ for $S \cong 1.24$ as opposed to $Ra_{cr2} \cong 25\,570$ for $S \cong 1$). Overall, this figure provides a good indication of the tendency of the system to support higher amplitudes (e_1) as the volume becomes larger (which is consistent with the corresponding increase in the physical space that the vortex has at its disposal to move back and forth along the horizontal direction). To complement this scenario with additional relevant data, Fig. 25 shows the flow frequency as a function of the Rayleigh number.

Having completed quite an exhaustive description of these aspects in the case of convex liquid bridge, in the following, the focus is shifted to the situation in which the liquid bridge has essentially a concave shape ($S < 1$).

As one may expect on the basis of a simple deductive approach (and the earlier observation that for $S > 1$, the roll displays an increased ability to undergo oscillations because of a larger degree of freedom in the horizontal direction), the experiments have confirmed that a shrinkage of the volume has just the opposite influence, i.e., it determines a significant contraction of the trajectories described by the roll center and a rise in the second critical Rayleigh number.

Unfortunately, given the minute spatial oscillations undergone by the roll center in proximity to the onset and the inability of the algorithm described in Sec. II F to properly capture them (with a sufficient resolution), for this case. Data comparable to those summarized in Fig. 24 could not be determined. Given this bottleneck, the information reported in the following have, therefore, been obtained through visual inspection of the overall flow pattern contained in the videos recorded during the execution of the experiment (from which we could infer that for $S = 0.7$, the critical $\Delta T \cong 54\text{ K}$ and the corresponding $Ra_{cr2} \cong 3.29 \times 10^4$).

That is why in the remainder of this section we rely on a different approach to get additional useful insights into these phenomena, that is, we examine the dynamics at fixed Ra for values of S spanning the



a)

b)

FIG. 25. (a) Non-dimensional frequency as a function of Ra for $A = 0.7$, $S \cong 1.24$ ($Bo \cong 1.65$), and snapshot of the related convex (fat) liquid bridge (b). The frequency has been made non-dimensional using the thermal diffusion time based on the liquid bridge height (L^2/α). The spline is used to guide the eye.

range between 0.7 and 1.3 and a fixed ΔT sufficiently high to make the amplitude e_1 appreciable in all cases. The outcome of this way of thinking are shown in Fig. 26 where we have included the vortex center trajectories for $\Delta T = 60$ K and different values of S .

The remarkable decrease undergone by the loop area for decreasing values of S is very evident in this series of panels. Figure 27 simply provides the corresponding changes in the vortex oscillation frequency. It is instrumental in showing that, although a smaller volume of liquid

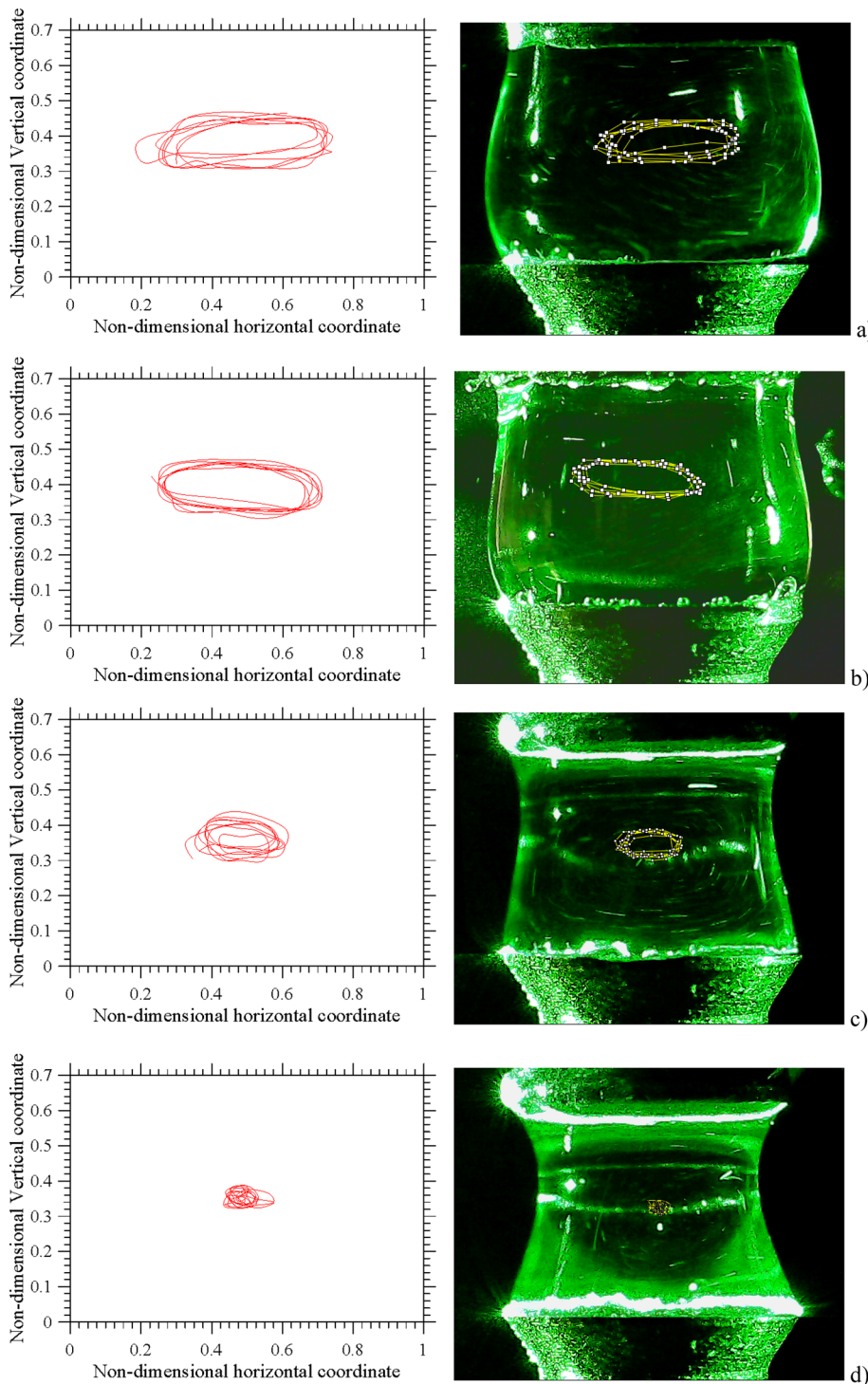


FIG. 26. Vortex center trajectory in the meridian plane for $A=0.7$, $Bo \cong 1.65$, $\Delta T=60$ K (T_{cold} fixed to 5°C , $Ra=36\,530$), and various volumes: (a) $S \cong 1.15$, (b) $S \cong 1.04$, (c) $S \cong 0.88$, and (d) $S \cong 0.7$.

16 May 2024 12:37:44

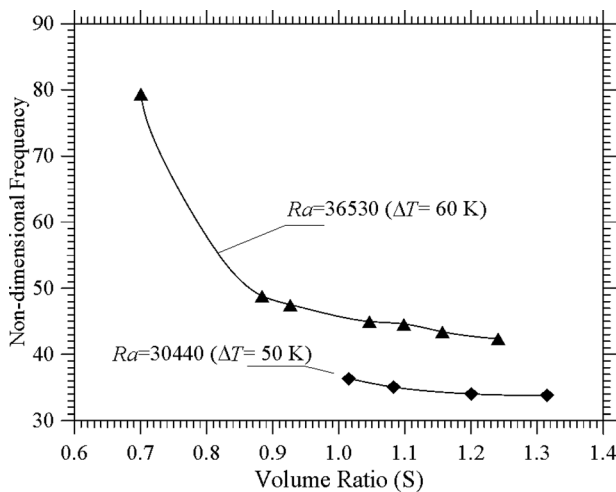


FIG. 27. Non-dimensional frequency as a function of the volume ratio (S) for $A = 0.7$ and two different values of the Rayleigh number.

essentially causes a shrinkage of the vortex (spatial) oscillation amplitude (given the more restrictive geometrical conditions the vortex is subjected to), however, it leads to a notable increase in the flow oscillation frequency, especially if values of S smaller than 0.8 are considered.

IV. CONCLUSIONS

The heretofore poorly investigated properties of buoyant convection in liquid bridges heated from below have been investigated experimentally by means of a microscale apparatus by which the size of the liquid column can be minimized, thereby enabling the liquid surface tension to balance the effects of gravity. Different modes of convection have been revealed, which differ in regard to the multiplicity of rolls being created in the bulk of the liquid and the related hierarchy of bifurcations.

While for relatively shallow liquid bridges, multi-cellular structures are visible in a specific meridian plane where tracers are properly illuminated by means of laser-cut technique, the flow reduces to the classical $m = 1$ structure with fluid rising along one side of the liquid bridge and sinking at the opposite side when the aspect ratio exceeds a given threshold.

Interestingly, some aspect ratios exist ($A = 0.3$ and $A = 0.6$) for which multiple solutions are possible, i.e., the emerging steady flow can assume different configurations according to the initial conditions or if it is deliberately disturbed by external mechanical stimuli (i.e., artificially imposed re-mixing).

An increase in the applied temperature difference can make the initially steady flow oscillatory. Unlike the unstable modes of convection (traveling waves) typical of surface-tension driven flow in liquid bridges heated from above or from below or often seen in cylindrical enclosures uniformly heated from below and cooled from above, the hallmark of the oscillatory flow of buoyant nature emerging in liquid bridges for $m = 1$ is a kind of rocking motion visible in the meridian plane. Such a behavior simply consists of a rhythmic displacement of the vortex core.

This leads to the remarkable conclusion that, when the lateral wall is replaced by a free-slip boundary, traveling waves are no longer a solution to the problem (at least in the considered range of temperature differences). The absence of traveling waves is supported by two

independent facts or realizations: (1) closed particle streamlines can be observed in a fixed meridian plane only; on changing the illuminated plane, such a pattern is no longer recognizable (which confirms that no traveling wave is at play, otherwise such a convective structure would re-appear cyclically in a fixed observation plane), and (2) in all oscillatory cases, the roll sense of circulation never changes; if a roll is oriented in the clockwise direction, it always retains this sense of circulation even if its center undergoes a periodic displacement in time (this contradicts the typical dynamics in the case of traveling waves, where a given convective pattern should reappear with inverted sense of circulation periodically). However, the degrees of freedom associated with the observed purely rocking motion increase as the temperature difference and/or the aspect ratio of the liquid bridge become higher. These result in interesting morphological variations in the shape of the limit cycle (loop) or “attractor,” which is obtained in the physical space through proper tracking of the vortex core.

An increase/decrease in the effective volume of liquid held between the supporting disks has a multi-fold effect on such dynamics. While for a fixed value of the Rayleigh number, a larger S causes an expansion (in space) of the size of the aforementioned loop and a decrease in the frequency of oscillations, vice versa, a smaller S can make the frequency much higher and induce a significant shrinkage of the closed trajectory described by the vortex core. In the latter case, the degenerate situation in which the attractor (loop) is reduced to a point represents the limiting situation for which, on reducing S , a steady state is recovered.

Overall, the critical Rayleigh number for the onset of oscillations increases quadratically with the aspect ratio and displays an inverse dependence on the volume ratio (the larger S , the smaller Ra_{crit}).

This study leaves room for more experimental work aimed at extending this line of inquiry through consideration of non-Newtonian water-based (viscoelastic) fluids.

AUTHOR DECLARATIONS

Conflict of Interest

The authors have no conflicts to disclose.

Author Contributions

Ahmed Aljanadi: Data curation (lead); Investigation (equal); Methodology (equal); Validation (lead); Visualization (lead); Writing – review & editing (supporting). **Monica S. N. Oliveira:** Software (equal); Supervision (supporting); Writing – review & editing (supporting). **Marcello Lappa:** Conceptualization (lead); Formal analysis (equal); Investigation (equal); Methodology (equal); Project administration (lead); Resources (lead); Supervision (lead); Writing – original draft (lead); Writing – review & editing (equal).

DATA AVAILABILITY

The data that support the findings of this study are available from the corresponding author upon reasonable request.

REFERENCES

- ¹G. Muller, G. Neumann, and W. Weber, “Natural convection in vertical Bridgman configurations,” *J. Cryst. Growth* **70**, 78–93 (1984).
- ²M. J. Crochet, F. Dupret, Y. Ryckmans, F. T. Geyling, and E. M. Monberg, “Numerical simulation of crystal growth in a vertical Bridgman furnace,” *J. Cryst. Growth* **97**, 173–185 (1989).

- ³R. Bennacer, M. El Ganaoui, and E. Leonardi, "Vertical Bridgman configuration heated from below: 3D bifurcation and stability analysis," in *Third International Conference on CFD in the Minerals and Process Industries* (CSIRO, Melbourne, 2003).
- ⁴S. Arena, G. Cau, and C. Palomba, "CFD simulation of melting and solidification of PCM in thermal energy storage systems of different geometry," *J. Phys.: Conf. Ser.* **655**, 012051 (2015).
- ⁵M. B. Ben Hamid, F. Al Shammari, I. Altawi, M. Alhadri, M. A. Almehaal, and K. Hajlaoui, "Potential of tubular solar still with rectangular trough for water production under vacuum condition," *Therm. Sci.* **26**, 4271–4283 (2022).
- ⁶R. Azzouz and M. B. B. Hamida, "Natural convection in a circular enclosure with four cylinders under magnetic field: Application to heat exchanger," *Processes* **11**, 2444 (2023).
- ⁷M. Lappa, *Thermal Convection: Patterns, Evolution and Stability* (John Wiley & Sons, Ltd., Chichester, 2009).
- ⁸K. Borońska and L. S. Tuckerman, "Extreme multiplicity in cylindrical Rayleigh-Bénard convection: I. Time-dependence and oscillations," *Phys. Rev. E* **81**, 036320 (2010).
- ⁹K. Borońska and L. S. Tuckerman, "Extreme multiplicity in small aspect ratio Rayleigh-Bénard convection: II. Bifurcation diagram and symmetry classification," *Phys. Rev. E* **81**, 036321 (2010).
- ¹⁰M. Lappa and A. Boaro, "Rayleigh-Bénard convection in viscoelastic liquid bridges," *J. Fluid Mech.* **904**, A2 (2020).
- ¹¹S. Kimura and K. Kitamura, "Floating zone crystal growth and phase equilibria: A review," *J. Am. Ceram. Soc.* **75**(6), 1440–1446 (1992).
- ¹²S. M. Koohpayeh, D. Fort, and J. S. Abell, "The optical floating zone technique: A review of experimental procedures with special reference to oxides," *Prog. Cryst. Growth Charact. Mater.* **54**(3–4), 121–137 (2008).
- ¹³H. Riemann and A. Luedge, "Floating zone crystal growth," in *Crystal Growth of Si for Solar Cells* (Springer Berlin Heidelberg, Berlin, Heidelberg, 2009), pp. 41–53.
- ¹⁴J. Chen and D. E. Smith, "Filament rheological characterization for fused filament fabrication additive manufacturing: A low-cost approach," *Addit. Manuf.* **47**, 102208 (2021).
- ¹⁵A. Das, E. L. Gilmer, S. Biria, and M. J. Bortner, "Importance of polymer rheology on material extrusion additive manufacturing: Correlating process physics to print properties," *ACS Appl. Polym. Mater.* **3**(3), 1218–1249 (2021).
- ¹⁶M. Lappa, "On the stability and prominent features of Marangoni flow in classical models of the floating zone technique in normal and microgravity conditions," in *Studies on Flow Instabilities in Bulk Crystal Growth*, edited by A. Gelfgat (Transworld Research Network, 2007), pp. 83–128.
- ¹⁷M. Lappa, "Convective effects and traveling waves in transparent oxide materials processed with the floating zone technique," in *Recent Studies in Materials Science*, edited by P. R. Lind (Nova Science Publishers Inc., 2019), pp. 97–150.
- ¹⁸R. Savino, R. Monti, M. Lappa, L. Carotenuto, D. Castagnolo, and R. Fortezza, "Flight results on Marangoni flow instability in liquid bridges," *Acta Astronaut.* **47**(2–9), 325–334 (2000).
- ¹⁹Q. Kang, D. Wu, L. Duan, L. Hu, J. Wang, P. Zhang, and W. Hu, "The effects of geometry and heating rate on thermocapillary convection in the liquid bridge," *J. Fluid Mech.* **881**, 951–982 (2019).
- ²⁰F. Preisser, D. Schwabe, and A. Scharmann, "Steady and oscillatory thermocapillary convection in liquid columns with free cylindrical surface," *J. Fluid Mech.* **126**, 545–567 (1983).
- ²¹S. Frank and D. Schwabe, "Temporal and spatial elements of thermocapillary convection in floating zones," *Exp. Fluids* **23**, 234–251 (1997).
- ²²R. Monti, R. Savino, and M. Lappa, "Influence of geometrical aspect ratio on the oscillatory Marangoni convection in liquid bridges," *Acta Astronaut.* **47**(10), 753–761 (2000).
- ²³I. Ueno, S. Tanaka, and H. Kawamura, "Oscillatory and chaotic thermocapillary convection in a half-zone liquid bridge," *Phys. Fluids* **15**(2), 408–416 (2003).
- ²⁴Y. Abe, I. Ueno, and H. Kawamura, "Effect of shape of HZ liquid bridge on particle accumulation structure (PAS)," *Microgravity Sci. Technol.* **19**(3), 84–86 (2007).
- ²⁵M. Gotoda, D. E. Melnikov, I. Ueno, and V. Shevtsova, "Experimental study on dynamics of coherent structures formed by inertial solid particles in three-dimensional periodic flows," *Chaos* **26**(7), 073106 (2016).
- ²⁶R. Velten, D. Schwabe, and A. Scharmann, "The periodic instability of thermocapillary convection in cylindrical liquid bridges," *Phys. Fluids A* **3**, 267–279 (1991).
- ²⁷M. Lappa, R. Savino, and R. Monti, "Influence of buoyancy forces on Marangoni flow instabilities in liquid bridges," *Int. J. Numer. Methods Heat Fluid Flow* **10**(7), 721–749 (2000).
- ²⁸R. Touihri, H. Ben Hadid, and D. Henry, "On the onset of convective instabilities in cylindrical cavities heated from below. I. Pure thermal case," *Phys. Fluids* **11**(8), 2078–2088 (1999).
- ²⁹M. Gotoda, A. Toyama, M. Ishimura, T. Sano, M. Suzuki, T. Kaneko, and I. Ueno, "Experimental study of coherent structures of finite-size particles in thermocapillary liquid bridges," *Phys. Rev. Fluids* **4**(9), 094301 (2019).
- ³⁰W. Thielicke and E. J. Stamhuis, "PIVlab—Towards user-friendly, affordable and accurate digital particle image velocimetry in MATLAB," *J. Open Res. Software* **2**, e30 (2014).
- ³¹S. M. Pizer, E. P. Amburn, J. D. Austin, R. Cromartie, A. Geselowitz, T. Greer, B. ter Haar Romeny, J. B. Zimmerman, and K. Zuiderveld, "Adaptive histogram equalization and its variations computer vision," *Graph. Image Process.* **39**, 355–368 (1987).
- ³²J. Soria, "An investigation of the near wake of a circular cylinder using a video-based digital cross-correlation particle image velocimetry technique," *Exp. Therm. Fluid Sci.* **12**, 221–233 (1996).
- ³³J. Westerweel, D. Dabiri, and M. Gharib, "The effect of a discrete window offset on the accuracy of cross-correlation analysis of digital PIV recordings," *Exp. Fluids* **23**, 20–28 (1997).
- ³⁴N. Chenouard, I. Smal, F. De Chaumont, M. Maška, I. F. Szbalzarini, Y. Gong, and E. Meijering, "Objective comparison of particle tracking methods," *Nat. Methods* **11**(3), 281–289 (2014).
- ³⁵Y. Yamaguchi, C. J. Chang, and R. A. Brown, "Multiple buoyancy-driven flows in a vertical cylinder heated from below," *Philos. Trans. R. Soc. London Ser. A: Math. Phys. Sci.* **312**(1523), 519–552 (1984).
- ³⁶V. Croquette, M. Mory, and F. Schosseler, "Rayleigh-Bénard convective structures in a cylindrical container," *J. Phys. France* **44**(3), 293–301 (1983).
- ³⁷V. Croquette, P. Le Gal, and A. Pocheau, "Spatial features of the transition to chaos in an extended system," *Phys. Scr.* **T13**, 135–138 (1986).
- ³⁸V. Croquette, "Convective pattern dynamics at low Prandtl number: Part I," *Contemp. Phys.* **30**(2), 113–133 (1989).
- ³⁹V. Croquette, "Convective pattern dynamics at low Prandtl number: Part II," *Contemp. Phys.* **30**(3), 153–171 (1989).
- ⁴⁰E. Crespo Del Arco and P. Bontoux, "Numerical simulations and analysis of axisymmetric convection in a vertical cylinder: An effect of Prandtl number," *Phys. Fluids* **1**, 1348–1359 (1989).
- ⁴¹E. Crespo Del Arco, P. Bontoux, R. L. Sani, G. Hardin, and G. P. Extrémet, "Steady and oscillatory convection in vertical cylinders heated from below. Numerical simulation of asymmetric flow regimes," *Adv. Space Res.* **8**(12), 281–292 (1988).
- ⁴²G. Neumann, "Three-dimensional numerical simulation of buoyancy driven convection in vertical cylinders heated from below," *J. Fluid Mech.* **214**, 559–578 (1990).
- ⁴³G. R. Hardin and R. L. Sani, "Buoyancy-driven instability in a vertical cylinder: Binary fluids with Soret effect. Part 2: Weakly non-linear solutions," *Numer. Methods Fluids* **17**, 755–786 (1993).
- ⁴⁴C. Wagner, R. Friedrich, and R. Narayanan, "Comments on the numerical investigation of Rayleigh and Marangoni convection in a vertical cylinder," *Phys. Fluids* **6**, 1425–1433 (1994).
- ⁴⁵B. Hof, G. J. Lucas, and T. Mullin, "Flow state multiplicity in convection," *Phys. Fluids* **11**, 2815–2817 (1999).
- ⁴⁶T. C. Cheng, Y. H. Li, and T. F. Lin, "Effects of thermal boundary condition on buoyancy driven transitional air flow in a vertical cylinder heated from below," *Numer. Heat Transfer A: Appl.* **37**(8), 917–936 (2000).
- ⁴⁷S. S. Leong, "Numerical study of Rayleigh-Bénard convection a cylinder," *Numer. Heat Transfer A* **41**, 673–683 (2002).
- ⁴⁸K. Borońska and L. S. Tuckerman, "Standing and travelling waves in cylindrical Rayleigh-Bénard convection," *J. Fluid Mech.* **559**, 279–298 (2006).
- ⁴⁹H. Jeffreys, "The stability of a fluid layer heated from below," *Philos. Mag.* **2**, 833–844 (1926).
- ⁵⁰M. Wanschura, H. C. Kuhlmann, and H. J. Rath, "Three-dimensional instability of axisymmetric buoyant convection in cylinders heated from below," *J. Fluid Mech.* **326**, 399–415 (1996).
- ⁵¹L.-S. Yao, "Multiple solutions in fluid dynamics," *Nonlinear Anal. Model. Control* **14**(2), 263–279 (2009).

- ⁵²J. Kengne, A. Nguomkam Negou, D. Tchiotsop, V. Kamdoun Tamba, and G. H. Kom, "On the dynamics of chaotic systems with multiple attractors: A case study," in *Recent Advances in Nonlinear Dynamics and Synchronization. Studies in Systems, Decision and Control*, edited by K. Kyamakya, W. Mathis, R. Stoop, J. Chedjou, and Z. Li (Springer, Cham, 2018), Vol. 109.
- ⁵³S. K. S. Boetcher, *Natural Convection from Circular Cylinders* (Springer, New York, 2014).
- ⁵⁴J. W. Song and L. W. Fan, "Temperature dependence of the contact angle of water: A review of research progress, theoretical understanding, and implications for boiling heat transfer," *Adv. Colloid Interface Sci.* **288**, 102339 (2021).
- ⁵⁵P. Bergè, Y. Pomeau, and C. Vidal, *Order Within Chaos—Towards a Deterministic Approach to Turbulence* (John Wiley, New York, 1984).
- ⁵⁶W. R. Hu, J. Z. Shu, R. Zhou, and Z. M. Tang, "Influence of liquid bridge volume on the onset of oscillation in floating zone convection. I. Experiments," *J. Cryst. Growth* **142**, 379–384 (1994).
- ⁵⁷W. R. Hu, Z. M. Tang, J. Z. Shu, and R. Zhou, "Influence of liquid bridge volume on the critical Marangoni number in thermocapillary convection of half floating zone," *Microgravity Q.* **5**(2), 67–74 (1995).
- ⁵⁸W. R. Hu and Z. M. Tang, "Influence of liquid bridge volume on the floating zone convection," *Cryst. Res. Technol.* **38**(7–8), 627–634 (2003).
- ⁵⁹A. Hirata, S. Nishizawa, and M. Sakurai, "Experimental results of oscillatory Marangoni convection in a liquid bridge under normal gravity," *J. Jpn. Soc. Microgravity Appl.* **14**, 122–129 (1997).
- ⁶⁰A. Hirata, M. Sakurai, and N. Ohishi, "Effect of gravity on Marangoni convection in a liquid bridge," *J. Jpn. Soc. Microgravity Appl.* **14**, 130–136 (1997).
- ⁶¹A. Hirata, M. Sakurai, N. Ohishi, M. Koyama, T. Morita, and H. Kawasaki, "Transition process from laminar to oscillatory Marangoni convection in a liquid bridge under normal and microgravity," *J. Jpn. Soc. Microgravity Appl.* **14**, 137–143 (1997).